

MSc Biomedical Engineering

Antibacterial Surfaces Bearing Silver and Zinc Nanoparticles on Additively Manufactured Titanium Implants

Master Thesis

Niko Eka Putra

Delft University of Technology

Supervisor: Ir. Ingmar A. J. van Hengel
Dr. Ir. Iulian Apachitei
Prof. Dr. Ir. Amir A. Zadpoor

 **TU Delft** Delft
University of
Technology

Antibacterial Surfaces Bearing Silver and Zinc Nanoparticles on Additively Manufactured Titanium Implants

By

Niko Eka Putra

4613163

in partial fulfilment of the requirements for the degree of

Master of Science

in Biomedical Engineering

at the Delft University of Technology

to be defended publicly on Tuesday, August 28, 2018, at 11:00 AM

Supervisors:

Ir. Ingmar A. J. van Hengel

Dr. Ir. Iulian Apachitei

Prof. Dr. Ir. Amir A. Zadpoor

Biomaterials and Tissue Biomechanics Specialization

Biomechanical Engineering Department

Faculty of Mechanical, Maritime, and Materials Engineering

Delft University of Technology

Abstract

Background. The emergence of antibiotic-resistant bacteria has increased the number of implant revision procedures in the Netherlands due to implant-associated infections (IAI). *Staphylococci* strains accounted for more than 50% of all IAI cases. Preventative measure, such as active antibacterial surfaces on the implant, are urgently needed. This study aims to synthesize and characterize antibacterial surfaces containing silver nanoparticles (Ag NPs) and pure zinc nanoparticles (Zn NPs) on selective laser melting (SLM) Ti6Al4V implants, and evaluate the *in vitro* antibacterial properties against methicillin-resistant *Staphylococcus Aureus* (MRSA).

Methods. Porous SLM Ti6Al4V implants were biofunctionalized using plasma electrolytic oxidation (PEO) surface modification technique with calcium and phosphorus-based electrolyte bearing combinations of Ag NPs and pure Zn NPs. After PEO processing, the surface morphology and chemical compositions of the implant surface was analyzed using scanning electron microscopy (SEM) and energy dispersive X-ray spectroscopy (EDS). The Ag⁺ and Zn²⁺ ion release kinetics were measured for 28 days and hydroxyl ([•]OH) radical generation was determined using electron paramagnetic resonance (EPR) for 150 minutes. Finally, *in vitro* antibacterial properties were evaluated against MRSA.

Results. PEO processing resulted in implant surfaces with seven different Ag NPs and pure Zn NPs ratios with interconnected micro/nano-porous surface. The presence of Ag NPs and pure Zn NPs on the implants surface was confirmed with SEM and EDS analysis. The Ag⁺ and Zn²⁺ ion release accumulated over time, up to 28 days. From the measured ion release kinetics, the addition of Ag NPs stimulated the Zn²⁺ ion release in early hours in the implant groups with Ag NPs and pure Zn NPs combinations. Antibacterial mechanisms through the [•]OH radical generations were also detected in all PEO-modified groups, with PT-Zn generating the highest intensity. The antibacterial properties demonstrated comparable inhibition zones between PT-Ag and implant groups with Ag NPs and pure Zn NPs combinations, while no inhibition zone was observed in PT-Zn. Bactericidal properties against adherent MRSA were observed on PT-Ag and implant groups with Ag NPs and pure Zn NPs combinations, while only PT-Ag Zn 75 25, PT-Ag, and PT-Ag Zn killed the non-adherent MRSA. As well, prevention against MRSA biofilm formation for 24 hours were observed only in PT-Ag and the implants groups with Ag NPs and pure Zn NPs combinations.

Conclusion. Antibacterial surfaces bearing Ag NPs and pure Zn NPs on porous SLM Ti6Al4V implants demonstrated promising *in vitro* antibacterial properties, which should be further developed for prevention of IAI in clinical applications.

Contents

1	Introduction	1
2	Materials and Methods	3
2.1	Study outline	3
2.2	Selective laser melting Ti6Al4V implants	3
2.3	Characterization of Ag and pure Zn nanoparticles	4
2.3.1	Scanning electron microscopy	4
2.3.2	X-ray diffraction	4
2.3.3	Particle size distribution and zeta potential analysis	4
2.4	Implant surface biofunctionalization	4
2.4.1	Experimental PEO setup	4
2.4.2	Synthesis of antibacterial TiO ₂ surface bearing Ag NPs and pure Zn NPs	5
2.5	Biomaterial characterization of biofunctionalized SLM implants	7
2.5.1	Scanning electron microscopy and energy dispersive X-ray spectroscopy	7
2.5.2	Inductively coupled plasma optical emission spectrometry	7
2.5.3	Electron paramagnetic resonance spectrometer	7
2.6	Antibacterial <i>in vitro</i> assays	8
2.6.1	Preparation of bacteria inoculum	8
2.6.2	Agar diffusion method	8
2.6.3	Minimum inhibitory and bactericidal concentration	9
2.6.4	Adherent and non-adherent CFU counts	10
2.6.5	Biofilm formation and characterization	12
2.7	Statistical analysis	12
3	Results	13
3.1	Characteristics of Ag and Zn nanoparticles	13
3.1.1	Particle morphology and phase compositions	13
3.1.2	Zeta potential and hydrodynamic size distribution in PEO electrolyte	14
3.2	PEO surface biofunctionalization	15
3.2.1	Electrical conductivity of PEO electrolyte	15
3.2.2	Voltage-time transients during PEO experiments	16

3.3 Surface characteristics of biofunctionalized SLM implants	17
3.3.1 Surface morphology of biofunctionalized SLM implants	17
3.3.2 Distribution of Ag NPs and pure Zn NPs in TiO ₂ surface	17
3.4 Ag ⁺ and Zn ²⁺ ion release kinetics	22
3.5 Hydroxyl radical generation	26
3.6 <i>In vitro</i> antibacterial activity of SLM implants	28
3.6.1 Inhibition zones	28
3.6.2 Minimum inhibitory and bactericidal concentration of AgNO ₃ and Zn(NO ₃) ₂	29
3.6.3 Bactericidal activity against adherent and non-adherent MRSA	30
3.6.4 Anti-biofilm activity	31
4 Discussion	35
4.1 Discussion of the results	35
4.2 Recommendations for future work	44
5 Conclusions	45
6 Acknowledgements	46
7 Abbreviations	47
8 References	48
9 Appendices	56

1 Introduction

As the number of total joint arthroplasty procedures increases each year, the revision surgeries due to complications is expected to rise [1], [2]. According to the Dutch arthroplasty registry, there were 29,520 total hip arthroplasty (THA) and 27,918 total knee arthroplasty (TKA) procedures performed in 2016 in the Netherlands. Over the past six years, this number has increased more than 20% and is predicted to keep growing in the future [2]–[4]. In the Netherlands, about 2.5% THA and 2% TKA procedures have resulted in revision surgeries due to infection [3]. Implant-associated infection (IAI) is the second biggest cause of implant failures.

The attachment of bacteria to the implant surface determines early IAI pathogenesis [5]. Once bacteria successfully adhere to the implant surface, rapid proliferation and secretion of polysaccharide matrix will follow. This extracellular matrix facilitates the adhesion of multilayer-bacteria and biofilm formation [6]. The bacteria within the biofilm demonstrate a high tolerance to antibiotics and immune responses [7]. The majority of antibiotics have limited success in the elimination of biofilms [8]. Some reasons for this are that systemically intake antibiotics are not delivered directly to infections sites, hence influenced the prophylactic as well as the therapeutic outcomes [9], [10]. Also, bacteria in the biofilm could migrate to the peri-implant tissue, which enhances the probability of re-infection after a revision surgery [7], [11]. A solution to prevent the biofilm formation is to provide antibacterial surface on the orthopedic implant, which will prevent bacteria from adhering to the implant surface.

Staphylococci strains, which have developed a resistance to methicillin antibiotics, have caused more than 50% of IAI cases [12]–[16]. Due to the emergence of antibiotic-resistant pathogens, research into the use of inorganic nanoparticles, such as silver nanoparticles (Ag NPs) and zinc nanoparticles (Zn NPs), as antibacterial agents has increased [17]. Ag NPs have demonstrated bactericidal properties against various bacterial strains, including multidrug-resistant pathogenic bacteria [18]–[21]. Zn NPs also have been reported to possess antibacterial properties against various Gram-positive and Gram-negative bacteria [22]–[25]. Besides antibacterial properties, Zn NPs also stimulate bone regeneration by promoting the adhesion, proliferation, and differentiation of mesenchymal stem cells (MSCs) into osteoblastic cells [26], [27]. While both silver and zinc have individual antibacterial properties, recent studies have observed the synergism between silver and zinc, i.e. Ag NPs and Zn²⁺ ions in titanium implants, on both antibacterial and osteogenic properties [28]–[30]. Regarding the cytotoxicity to human MSCs, zinc is five times less toxic compared to silver [31], [32]. Therefore, by substituting silver with zinc, possible cytotoxicity can be compensated preventing reducing the antibacterial effects [28].

Titanium alloys have been widely used in orthopedic implants due to their excellent biocompatibility and mechanical properties [28]. With the growth of additive manufacturing, titanium implants, fabricated with selective laser melting (SLM), are able to induce bone regeneration through the highly porous implant design [33], [34]. Even though highly porous implants stimulate bone regeneration, the large surface area could potentially increase the risk of bacterial adhesion and biofilm initiation. To decrease the chances of bacterial adhesion and prevent biofilm formation, an antibacterial surface needs to be integrated into customized SLM titanium implants.

Antibacterial surfaces of SLM titanium implants have been fabricated using plasma electrolytic oxidation (PEO), an electrochemical surface modification technique. PEO converts titanium surface into an interconnected micro/nano- titanium oxide (TiO_2) porous layer in a single step process [35]. The resulting porous TiO_2 surface contains antibacterial nanoparticles, while the pores provide space for bone ingrowth. SLM titanium implants containing Ag NPs modified through PEO process have demonstrated antibacterial properties against methicillin-resistant *Staphylococcus aureus* (MRSA) *in vitro* and *ex vivo* [36]. To the best of our knowledge, the combination of Ag NPs and pure Zn NPs on additively manufactured SLM titanium has not yet been investigated. Therefore, this study aims to synthesize and characterize antibacterial surfaces containing Ag NPs and pure Zn NPs on SLM Ti6Al4V implants, and evaluate antibacterial properties against MRSA in *in vitro* experiments.

2 Materials and Methods

2.1 Study outline

The outline of the study is presented in **Figure. 1**.

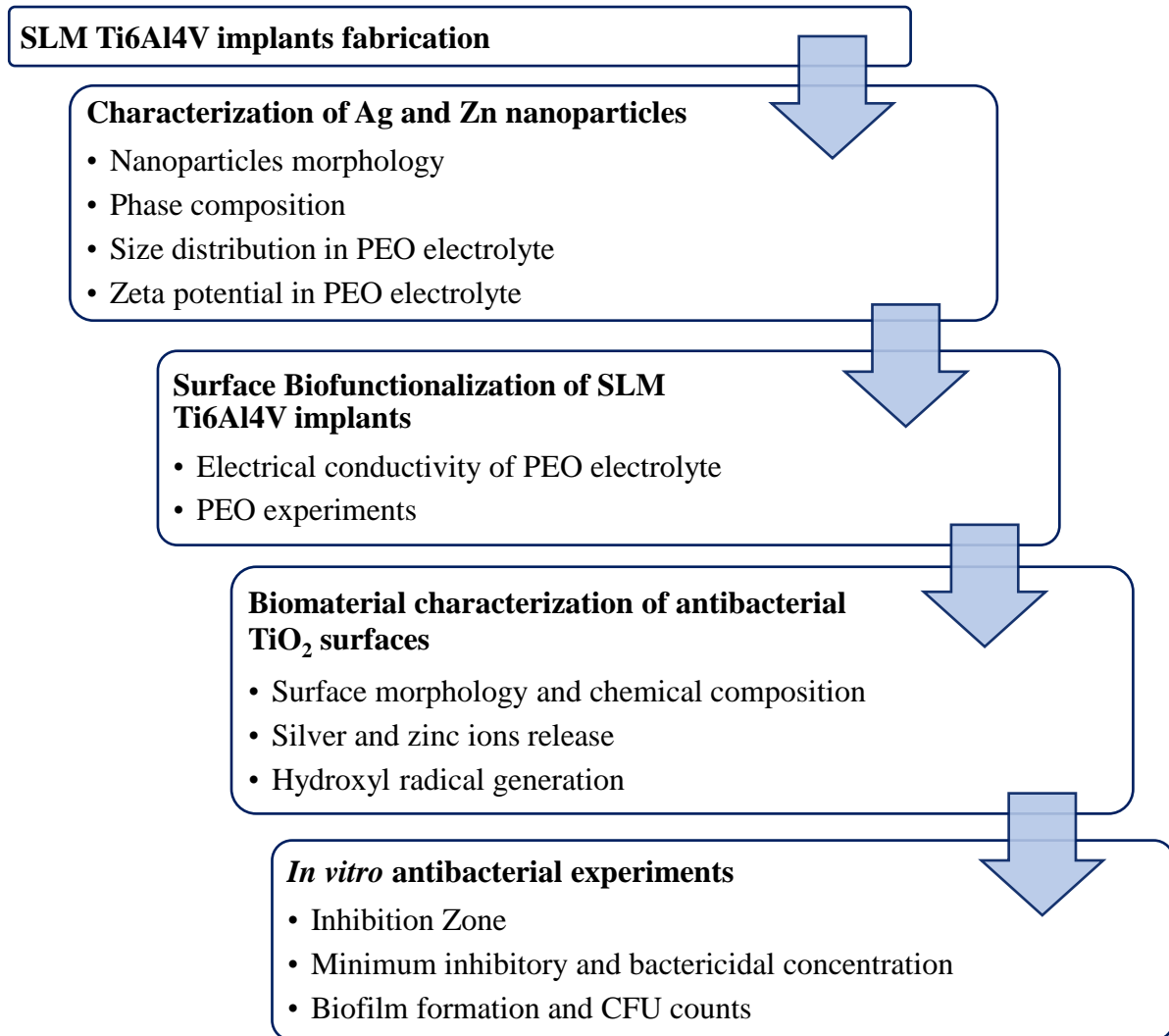


Figure. 1 Schematic representation of the study design.

2.2 Selective laser melting Ti6Al4V implants

The implants used in this study, were designed and fabricated by van Hengel et al. [36] in the Additive Manufacturing Lab (TU Delft, Delft, The Netherlands) using SLM device (SLM-125, Realizer, Borchem, Germany) with Ytterbium fiber laser (YLM-400-AC, IPG Photonics Corporation, Oxford, United States). The laser exposure time was 300 μ s, with 1070 \pm 10 nm wavelength and 96 W laser power. Medical grade (ELI, grade 23) Ti6Al4V powders (AP&C, Boisbriand, Quebec, Canada), with

spherical morphology and particle size 10-45 nm, were used as the materials for the fabrication. Furthermore, the as-manufactured SLM implants were ultrasonically cleaned in acetone, 96% ethanol, and demineralized water for 5 minutes each before PEO processing.

2.3 Characterization of Ag and pure Zn nanoparticles

2.3.1 Scanning electron microscopy

Particle morphology of Ag NPs and pure Zn NPs was observed using scanning electron microscopy (SEM) JSM-IT100 (JEOL, Tokyo, Japan), with an electron beam energy ranging from 5-20 kV and a working distance of 10 mm. Before imaging, the NPs were coated with a thin gold layer to improve the electrical conductivity.

2.3.2 X-ray diffraction

Phase composition of Ag NPs and pure Zn NPs was analyzed with X-ray diffraction (XRD). The analysis was performed using Bruker D8 Advance diffractometer (Bruker, Billerica, Massachusetts, United States) with Bragg-Brentano geometry and Lynxeye position sensitive detector. Cu K α radiation, divergence slit V12, and scatter screen height 5 mm were applied with the detector setting of LL 0.11 W 014, voltage: 45 kV, current: 40 mA, and 30 rpm sample spinning. The measurement was performed with a coupled θ -2 θ scan from 10 to 130°, with a step size of 0.030° 2 θ and counting time per 1-second step. Data were evaluated using Bruker software Diffrac Suite.EVA version 4.3.

2.3.3 Particle size distribution and zeta potential analysis in PEO electrolyte

Stability of Ag NPs and pure Zn NPs in PEO electrolyte was determined by size distribution and zeta potential measurements using Zetasizer Nano ZS (Malvern Panalytical, United Kingdom). The PEO electrolytes, containing Ag NPs and pure Zn NPs (**Table. 1**) were diluted 10 times before the measurements. 1 mL of the prepared suspension was taken using a syringe and injected into a disposable capillary cell, DTS1060. The size distribution and zeta potential measurements were performed 3 times with 10 runs each, at room temperature.

2.4 Implant surface biofunctionalization

2.4.1 Experimental PEO setup

The PEO experiments were conducted using a customized laboratory setup (**Figure. 2A**), at Surface Biofunctionalization Lab (TU Delft, Delft, The Netherlands). The setup consisted of an AC power supply (50Hz, type ACS 1500, ET Power Systems Ltd., United Kingdom), a PC interfaced with the

AC power supply through a data acquisition board (NI SCXI-1000, Austin, Texas, United States), and an electrolytic cell with two electrodes configuration (SLM Ti6Al4V implants as the anode and a cylindrical stainless-steel as a cathode), connected with a thermostatic bath (Thermo Haake V15, Karlsruhe, Germany) to maintain the temperature of the cell during the process.

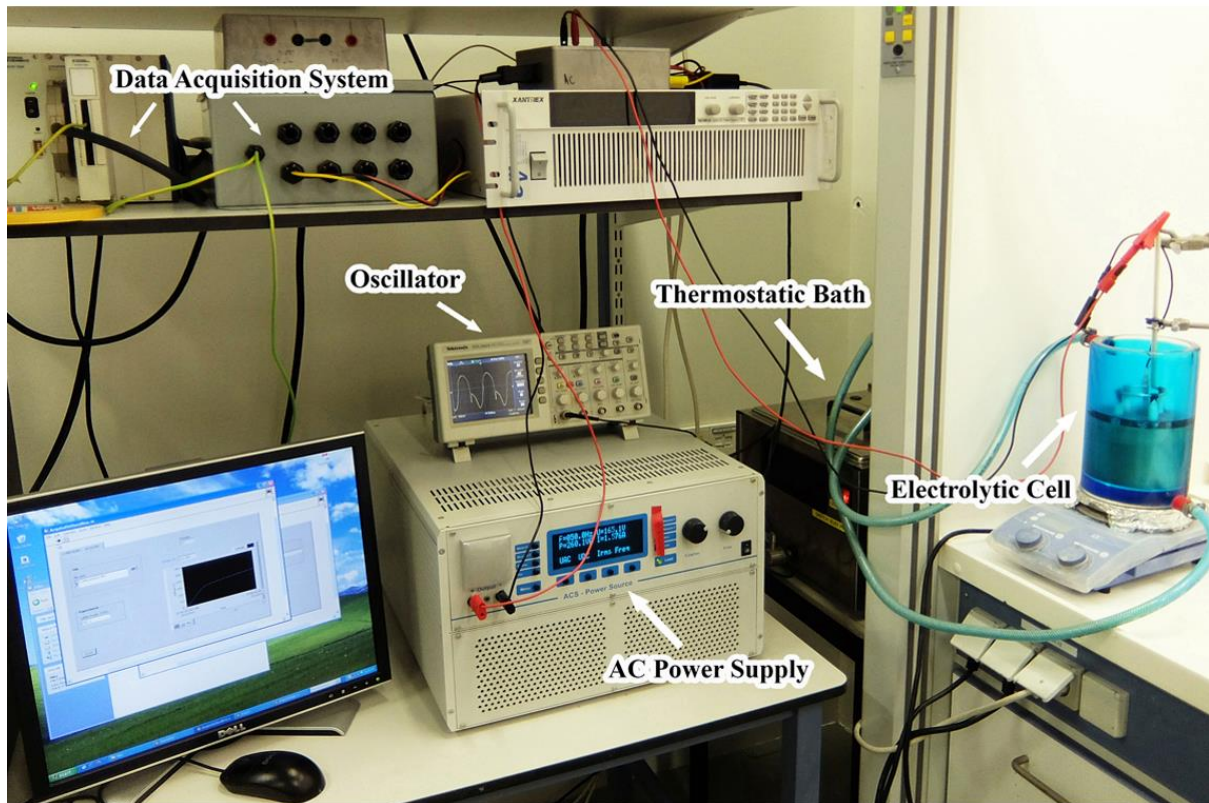
Table. 1 Experimental groups used in this study. SLM Ti6Al4V implants biofunctionalized with different concentrations of Ag NPs and pure Zn NPs in PEO electrolyte

Experimental groups	PEO electrolyte			
	Ag NPs (g/L)	Zn NPs (g/L)	Calcium acetate (g/L)	Calcium glycerophosphate (g/L)
Non-treated (NT)	–	–	–	–
PEO-treated (PT)	–	–	24	4.2
PT–Zn	–	3	24	4.2
PT–Ag Zn 25 75	0.75	2.25	24	4.2
PT–Ag Zn 50 50	1.5	1.5	24	4.2
PT–Ag Zn 75 25	2.25	0.75	24	4.2
PT–Ag	3	–	24	4.2
PT–Ag Zn	3	3	24	4.2

2.4.2 Synthesis of antibacterial TiO₂ surface bearing Ag NPs and pure Zn NPs

The PEO electrolyte was made of 4.2 g/L calcium glycerophosphate (Dr. Paul Lohmann GmbH, Emmerthal, Germany), 24 g/L calcium acetate hydrate (Sigma-Aldrich, St. Louis, United States), and different concentrations of Ag NPs and pure Zn NPs (Sigma-Aldrich, St. Louis, United States) dissolved in 800 mL demineralized water (**Table. 1**). The Ag NPs and pure Zn NPs had a size range in between 7-25 nm [37] and 40-60 nm, respectively. The NPs were dispersed in PEO electrolyte with 2 times ultrasonication for 5 minutes each and stirred in between, with 500 rotations per minute (rpm) for 5 minutes. Before PEO processing, the electrical conductivity of PEO electrolyte was measured using conductivity meter (Consort, Topac Inc., Cohasset, Massachusetts, United States).

A.



B.

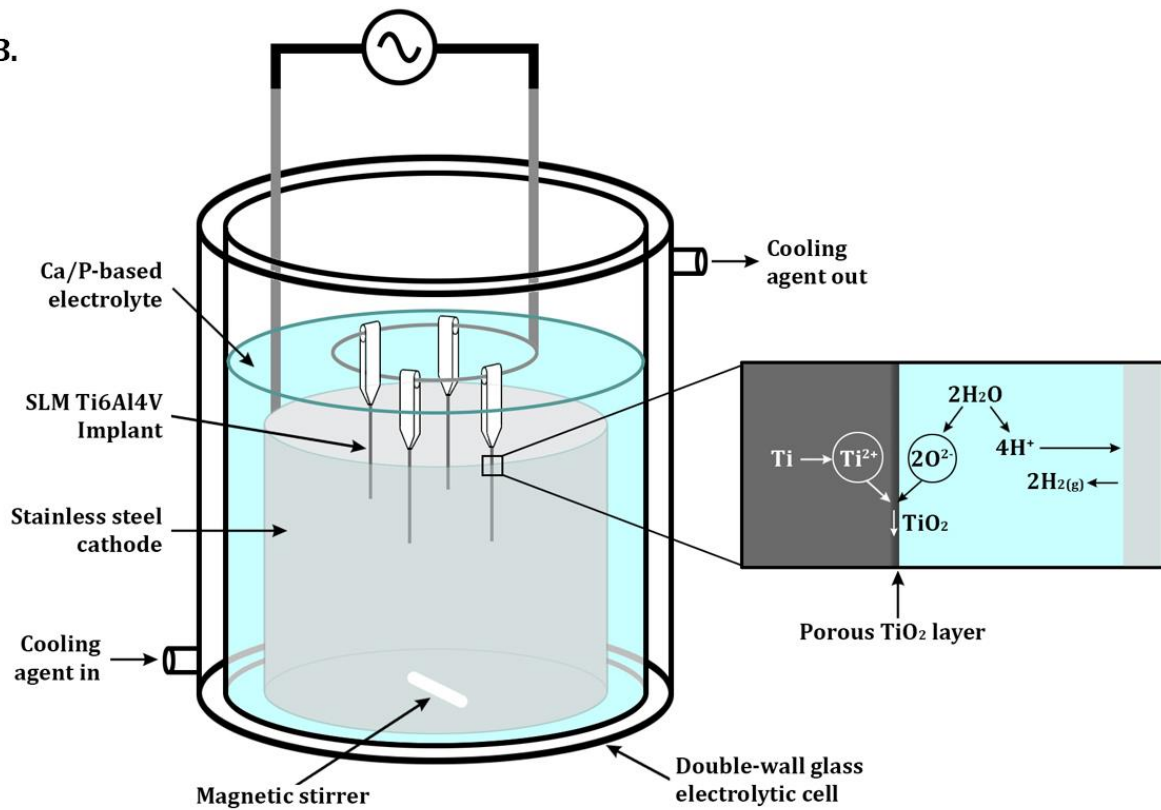


Figure. 2 A. Customized instruments setup for PEO experiments. B. Illustration of the PEO experiments performed in a double-wall glass electrolytic cell.

The PEO processing was conducted in the electrolytic cell (**Figure. 2B**). The electrolytic cell was filled with 800 mL of the PEO electrolyte containing Ag NPs and pure Zn NPs. Four SLM implants were fully-immersed in the electrolyte, surrounded by the cylindrical stainless-steel cathode inside the electrolytic cell. The experiments were performed for 300 seconds, under a galvanostatic condition, with a current density of 20 A/dm². Each experiment was started at a temperature of 6 ± 1°C. During the process, the electrolyte was stirred at 500 rpm to ensure the homogenous distribution of the nanoparticles. The voltage-time (V-t) transients were recorded with a sampling rate of 1 Hz. After PEO process, the implants were rinsed in running tap water for 1 minute to remove the residual electrolyte and unattached nanoparticles from the surface. Seven implant groups were synthesized in the process. Furthermore, the implants were sterilized by an hour heat treatment in an oven (UT6, Thermo Scientific Heraeus) at 110 °C, prior to *in vitro* antibacterial tests.

2.5 Biomaterial characterization of biofunctionalized SLM implants

2.5.1 Scanning electron microscopy and energy dispersive X-ray spectroscopy

Surface morphology and structure of the SLM implants were observed using SEM JSM-IT100 (JEOL, Tokyo, Japan), with an electron beam energy ranging from 5-20 kV and a working distance of 10 mm. Before imaging, the SLM implants were coated with a thin gold layer to improve the electrical conductivity. Furthermore, the chemical composition of a specific spot and surface area of the implants were analyzed using energy dispersive X-ray spectroscopy (EDS). The SEM imaging and EDS analysis was performed for all implant groups (**Table. 1**).

2.5.2 Inductively coupled plasma optical emission spectrometry

The Ag⁺ and Zn²⁺ ion release kinetics were studied by immersing 1.5 cm SLM implants bearing Ag NPs, pure Zn NPs, and the different combinations of both nanoparticles (n=3 per group) in 1 mL phosphate-buffered saline (PBS) (VWR Life Science, United States) solution in a dark Eppendorf tube. The tubes were kept in a water bath with a temperature of 37°C. The PBS solutions were collected and refreshed after 0.5, 1, 2, 4, 7, 14, and 28 days. Afterwards, Inductively coupled plasma-optical emission spectrometry (ICP-OES) was used to quantify the Ag⁺ and Zn²⁺ ion concentrations.

2.5.3 Electron paramagnetic resonance spectrometer

The radical generation from SLM implants surface was measured using Bruker EMX Plus, an X-band electron paramagnetic resonance (EPR) spectrometer (Billerica, Massachusetts, United States). The experiments were conducted at room temperature without any direct light illumination. The implant

was put inside a quartz capillary tube and inserted into the EPR spectrometer cavity. The EPR spectra were recorded after the settings were tuned. Two implants of each group with a length of 0.5 cm were prepared. One implant was used to record the baseline spectrum produced by the implant substrate, while the other was used to detect the radical generation. To detect the radicals, 10 μ L of 20 mM 5,5-dimethyl-pyrroline N-oxide (DMPO) (Sigma-Aldrich, St. Louis, United States), dissolved in PBS, was used as the trapping agent. The radical species covalently bonded with DMPO compounds to form longer-lived DMPO adducts that were detectable by the spectrometer.

Settings for the measurements were described as following: 9.78 GHz frequency, 4799.3 G sweep width to obtain the background spectrum of the implants, 100 G sweep width to detect the hydroxyl (\cdot OH) radical, 163.8 ms time constant, 160 ms conversion time, 1 G modulation amplitude, 100 kHz modulation frequency, 60 dB receiver gain, 10 dB attenuation, and 20 mW power. The radical generations were determined every 10 minutes for 150 minutes. The measurements were performed for all implant groups (**Table. 1**).

2.6 Antibacterial *in vitro* assays

2.6.1 Preparation of bacteria inoculum

To prepare a fresh bacteria inoculum, a single MRSA USA300 colony was suspended in 3 mL tryptic soy broth (TSB; UMC Utrecht, Utrecht, Netherlands) using a 1 μ L inoculation loop and incubated for about 3 hours at 37°C on a shaking platform with 120 rpm. After incubation, the bacterial optical density at 600 nm wavelength (OD_{600nm}) was measured using a spectrophotometer (GENESYS 20 Thermo Spectronic, Thermo Fisher Scientific, United States). The desired OD_{600nm} was between 0.1 and 0.5. The inoculum colonies were quantified by pipetting the 10 μ L of the ten-fold serial dilutions, from 10^0 to 10^{-6} , onto blood-agar plates (Becton Dickinson, Franklin Lakes, United States) and incubated overnight at 37 °C. Then, the CFU were quantified.

2.6.2 Agar diffusion method

The *in vitro* leaching activity of the SLM implants was observed through inhibition zones on Luria-Bertani (LB)-agar plates. First, the solid LB broth (UMC Utrecht, Utrecht, Netherlands) was boiled using a microwave and poured into sterile petri dishes. The petri dishes were cooled down at room temperature to solidify the LB broth. After that, a sterile cotton swab was used to equally distribute the fresh MRSA USA300 inoculum (OD_{600nm} 0.01, containing approximately 10^7 colony-forming unit (CFU)/mL bacteria) on the plates (**Figure. 3A**). The plate was turned 90° every swab (**Figure. 3B**), until each place was swapped twice, and bacteria completely covered the agar surface. Then, the

implants were placed on top of the LB-agar plates, (**Figure. 3C**), and incubated overnight at 37 °C. During incubation, the bacteria will grow and afterwards the inhibition zones can be observed (**Figure. 3D**). To quantify the inhibition zones, the plates were photographed using Image Quant LAS4000 (GE Healthcare). Subsequently, ImageJ software was used to quantify the inhibition zones. The experiments were performed for all implant groups (**Table. 1**), with the length of 1.5 cm and n=3 per group.

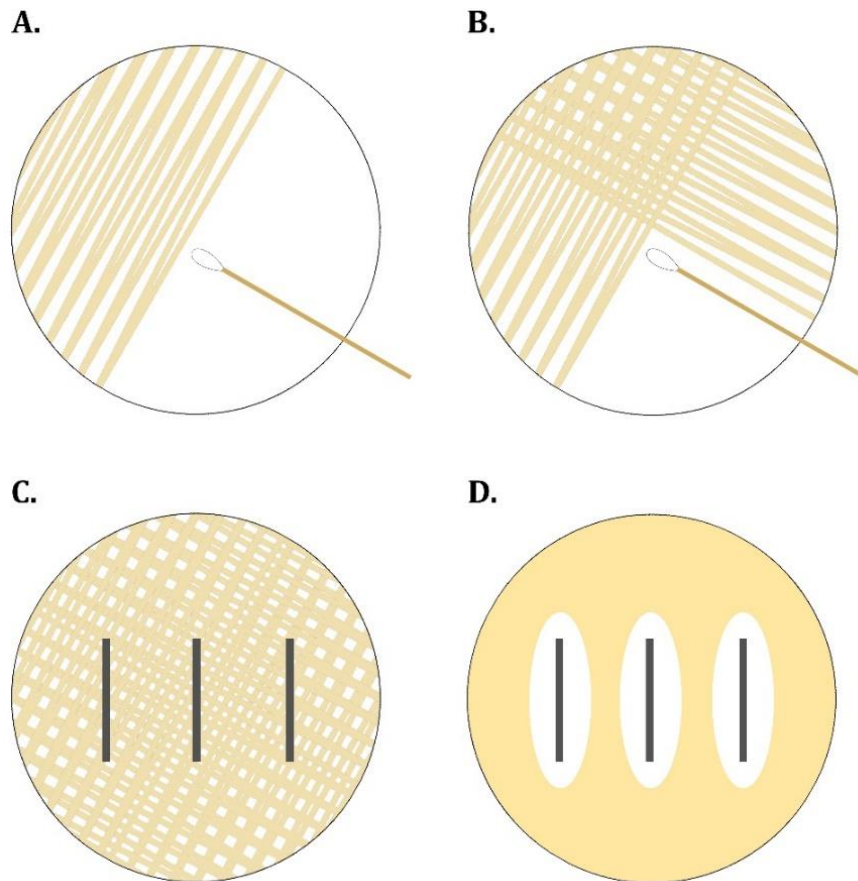


Figure. 3 An illustration of the agar diffusion method. **A.** Fresh MRSA USA300 inoculum containing approximately 10^7 CFU/mL were swabbed onto the LB-agar plate. **B.** The plate was turned 90 degrees every swab until the bacteria entirely covered the agar surface. **C.** Three implants were placed on the agar surface. **D.** After incubation for 24 hours at 37 °C, bacteria growth was observed, including colorless inhibition zones.

2.6.3 Minimum inhibitory and bactericidal concentration

To determine the minimum inhibitory and bactericidal concentration (MIC and MBC, respectively) of Ag^+ , Zn^{2+} ions, as well as the combinations, a fresh MRSA USA300 inoculum ($\text{OD}_{600\text{nm}}$ value of 0.09) was cultured in CAMH broth (UMC Utrecht, Utrecht, Netherlands) containing AgNO_3 (Sigma-Aldrich, St. Louis, United States) and $\text{Zn}(\text{NO}_3)_2$ (Sigma-Aldrich, St. Louis, United States).

First, AgNO_3 and $\text{Zn}(\text{NO}_3)_2$ were dissolved in CAMH broth and prepared with the start of 320 mM and 2 mM concentration, respectively. Two-fold serial dilutions of AgNO_3 , from 2 mM to 4 μM , and $\text{Zn}(\text{NO}_3)_2$, from 320 mM to 0.16 mM, were performed (**Figure. 4A**). After that, a fresh MRSA USA300 inoculum, prepared in CAMH broth, was pipetted to a 96-wells plate (**Figure. 4B**). Next, the bacteria were mixed with the antibacterial agents (**Figure. 4C**), and incubated statically overnight at 37°C. After incubation, visual turbidities can be observed (**Figure. 4D**). These turbidities indicated the growth of bacteria, while in the wells, where there were no turbidities, bacteria growth was inhibited. The MIC was noted at the lowest concentration where visual turbidities did not appear. Furthermore, to distinguish the bacteriostatic and bactericidal activity, 10 μL of the aliquots from each column were plated on blood-agar plates and incubated overnight at 37°C. Thereupon, the resulting bacteria colonies growth can be quantified to determine the MBC (**Figure. 4E**). The MBC was denoted where no colonies observed in the blood-agar plates.

2.6.4 Adherent and non-adherent CFU counts

To observe the bactericidal properties, the adherent and non-adherent MRSA USA300 were quantified after overnight incubation with the implants (**Table. 1**). Four implants of 1 cm each were incubated in a 100 μL of 10^2 and 10^3 CFU MRSA USA300, inside a 200 μL PCR tube, overnight at 37°C. The incubation process was conducted statically, and the tubes were placed in a horizontal position.

After incubation, the implants were taken out. The aliquots from the TSB medium were used to quantify the number of non-adherent bacteria. While, the implants were ultrasonicated for 1 minute, in a 200 μL PBS inside 0.5 mL Eppendorf tubes. The ultrasonication process allows the adherent bacteria to detach from the implants surface into the PBS medium. Subsequently, 10 μL of the aliquots of non-adherent bacteria and the PBS containing adherent bacteria were prepared in a serial dilution up to 10^{-6} and plated out in blood-agar plates and incubated overnight at 37°C. Thereby, the MRSA colonies were counted, and the CFU were quantified.

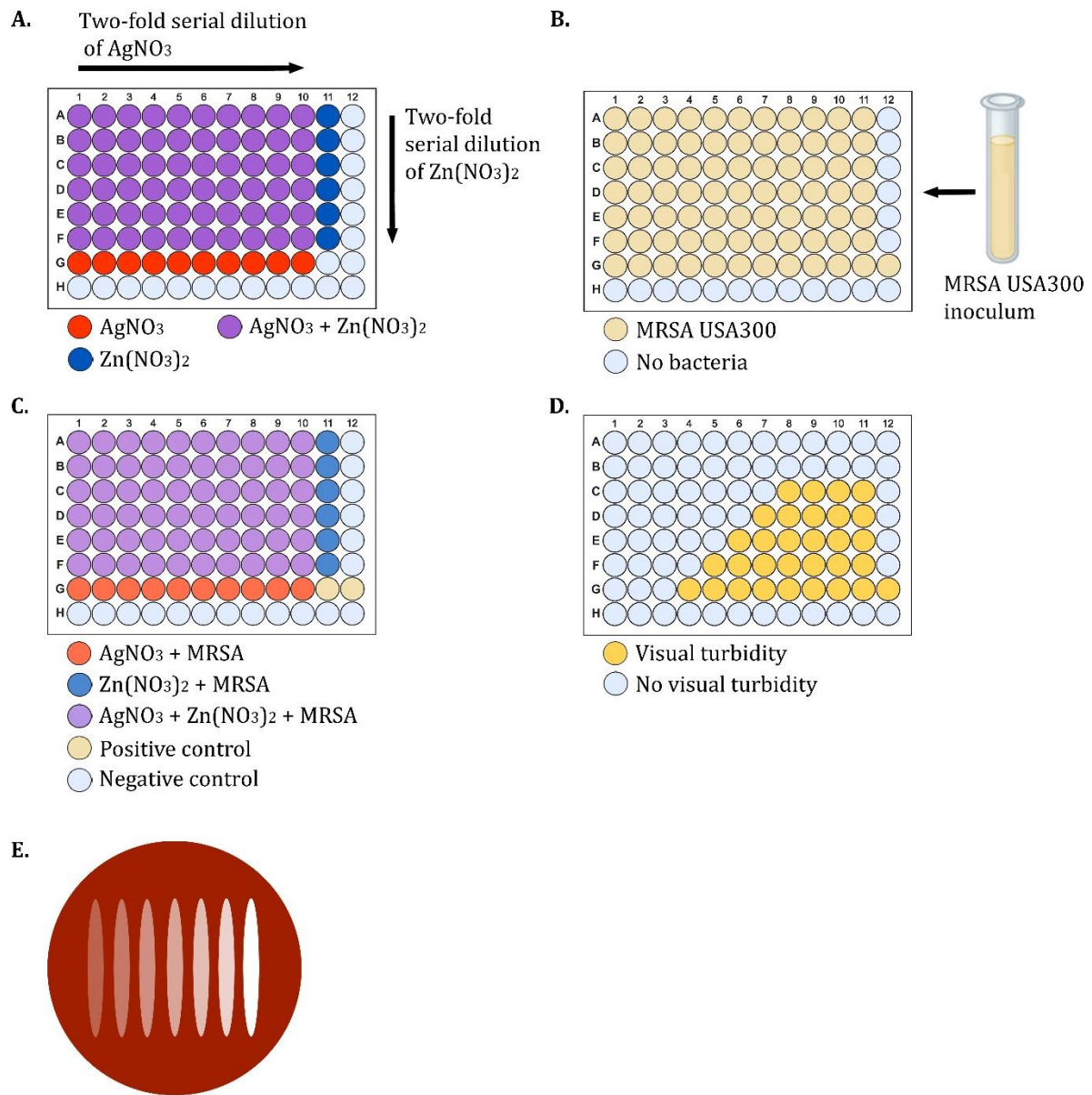


Figure. 4 An illustration of minimum inhibitory and bactericidal concentration experiment in 96-wells plates. **A.** Two-fold serial dilutions of AgNO_3 and $\text{Zn}(\text{NO}_3)_2$ and the combination of both were prepared in another 96-wells plate. **B.** Fresh MRSA USA300 inoculum was pipetted into the 96-wells plates. **C.** The antibacterial agents and bacteria inoculum were homogeneously mixed. **D.** After 24 hours of incubation at 37°C , the visual turbidities can be observed, indicating bacteria growth. **E.** Each column of the 96-wells plates was pipetted on the blood-agar plates to determine the minimal bactericidal concentration.

2.6.5 Biofilm formation and characterization

After 24 hours incubation at 37°C in 600 µL TSB medium, containing 1% glucose and 2×10^2 CFU MRSA USA300, the implants were fixed in McDowells fixative, containing 1% glutaraldehyde and 4% paraformaldehyde in 10 mM PBS at pH 7.4. After that, the implants were rinsed in demineralized water for 10 minutes, then dehydrated by submersion in 50% ethanol for 15 minutes, 70% ethanol for 20 minutes, 96% ethanol for 20 minutes, and hexamethyldisilazane for 30 minutes. Subsequently, the implants were left dried in air for about 2 hours and coated with gold layer prior to SEM imaging. The biofilm formation and characterization were performed for all implant groups (**Table. 1**), with the length of 1.5 cm and n=3 per group.

2.7 Statistical analysis

Graphical results were presented in mean \pm standard deviation. Statistical analysis was determined with GraphPad Prism (GraphPad Software, La Jolla, California, United States) using one-way ANOVA tests. Statistic significant between groups were considered at $p < 0.05$.

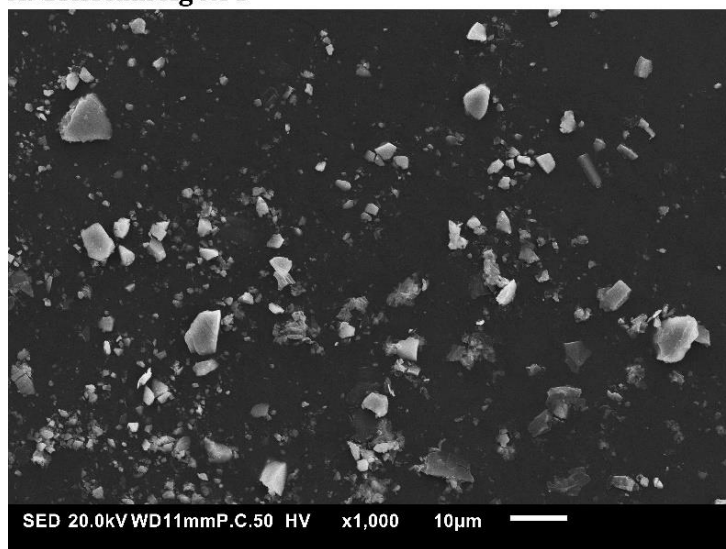
3 Results

3.1 Characteristics of Ag and Zn nanoparticles

3.1.1 Particle morphology and phase compositions

The as-purchased colloidal Ag NPs and pure Zn NPs were characterized with SEM and XRD for the particle morphology and phase composition. From the SEM images (**Figure. 5**), the colloidal Ag NPs appeared to be in irregular shape, while pure Zn NPs had spherical shape with size between 300 to 400 nm. The XRD spectra (**Figure. 6**) demonstrated only silver peaks but with a broad signal, whereas a minor intensity of zincite, were detected in pure Zn NPs.

A. Colloidal Ag NPs



B. Pure Zn NPs

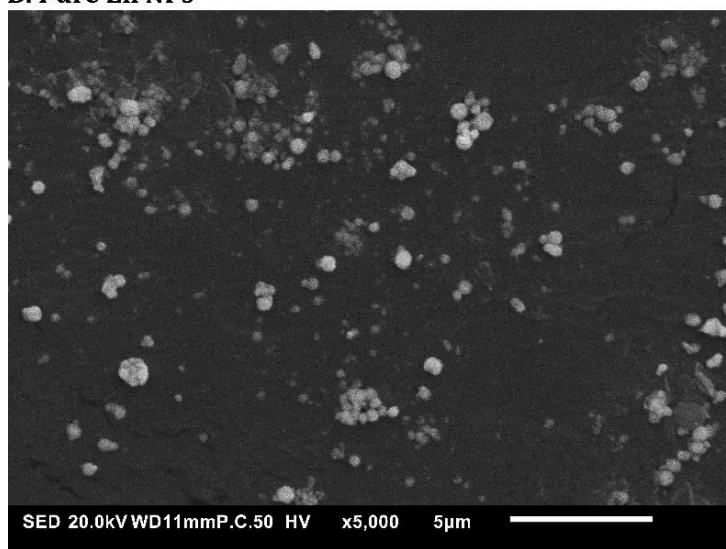


Figure. 5 Particle morphologies of **A.** colloidal Ag NPs and **B.** pure Zn NPs.

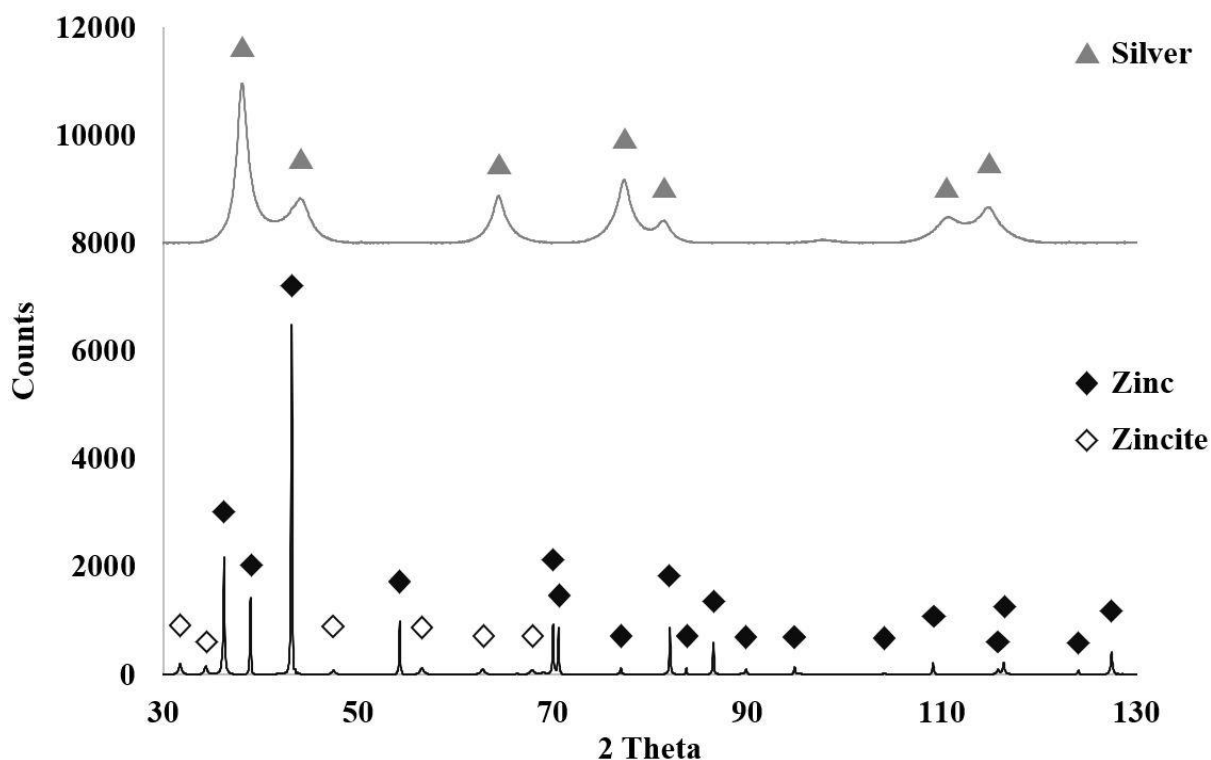


Figure. 6 Phase compositions of Ag NPs and pure Zn NPs.

3.1.2 Zeta potential and hydrodynamic size distribution in PEO electrolyte

Stability of Ag NPs and pure Zn NPs in PEO electrolyte were assessed through zeta potential and hydrodynamic size distribution measurements. The zeta potential values (Figure. 7) were in between -11 and -20 mV, where the numbers were close to agglomeration threshold [38], meaning that the NPs were relatively stable in PEO electrolyte. The results indicated that Ag NPs displayed better stability than pure Zn NPs. Also, the trend of zeta potentials in PEO electrolyte containing different combinations of the NPs showed an improve stability with a higher Ag NPs concentration.

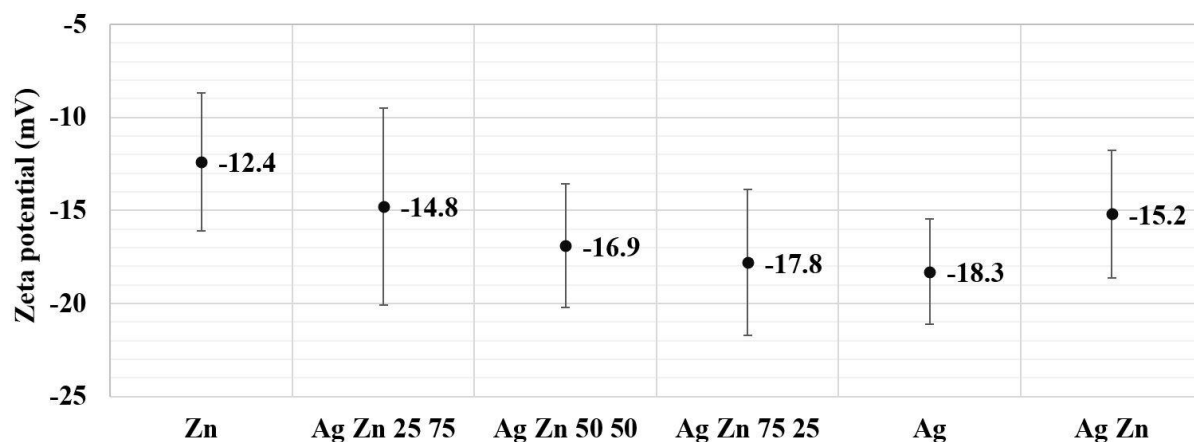


Figure. 7 Zeta potentials of Ag NPs and pure Zn NPs in PEO electrolyte (n=3 per group).

Hydrodynamic size distribution of Ag NPs and pure Zn NPs in PEO electrolyte showed that all NPs were not in the nano-size range or not smaller than 100 nm. Ag NPs had a larger particle size than pure Zn NPs (**Figure. 8**). The size distribution of the Ag NPs and pure Zn NPs combinations in PEO electrolyte also followed the trend, where a smaller particle size distribution was measured in the electrolyte with a higher pure Zn NPs concentration.

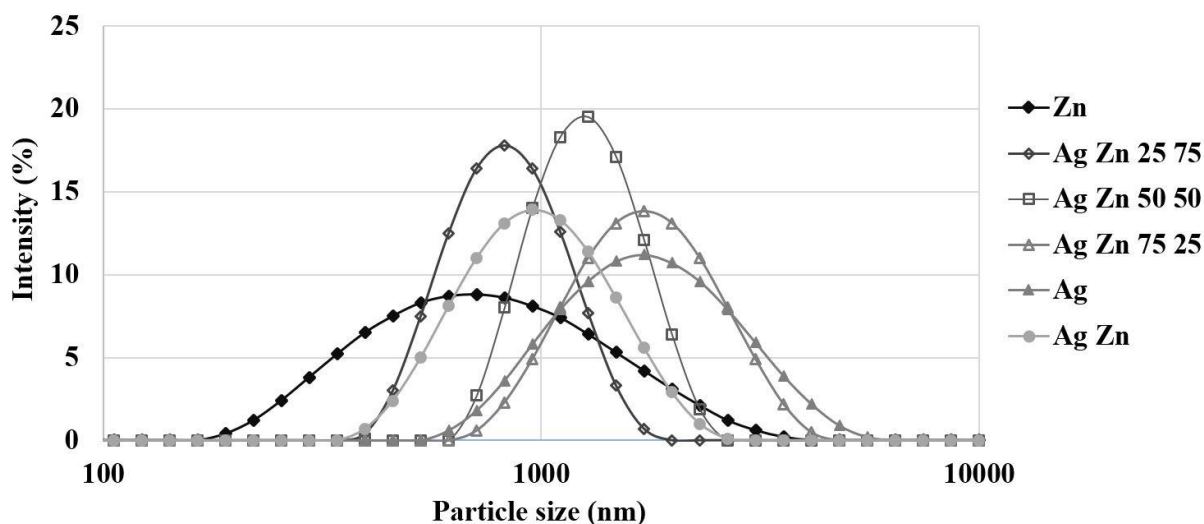


Figure. 8 Hydrodynamic size distributions of Ag NPs and pure Zn NPs in PEO electrolyte.

3.2 PEO surface biofunctionalization

3.2.1 Electrical conductivity of PEO electrolyte

The electrical conductivity of PEO electrolyte was measured by conductivity meter. The values were influenced by the addition of Ag NPs and pure Zn NPs. Higher electrical conductivity was achieved when the NPs were added due to more dissolved ions in the electrolyte (**Table. 2**).

Table. 2 Electrical conductivity of PEO electrolyte containing Ag NPs and pure Zn NPs.

Electrolyte	Electrical conductivity (mS/cm)
PEO electrolyte	10.43 ± 0.08
PEO electrolyte–Zn	13.96 ± 0.05
PEO electrolyte–Ag Zn 25 75	13.52 ± 0.04
PEO electrolyte–Ag Zn 50 50	13.33 ± 0.07
PEO electrolyte–Ag Zn 75 25	13.16 ± 0.06
PEO electrolyte –Ag	12.28 ± 0.08
PEO electrolyte –Ag Zn	14.04 ± 0.08

The addition of pure Zn NPs in PEO electrolyte resulted in a higher electrical conductivity compared with Ag NPs, indicated that pure Zn NPs dissolved better in PEO electrolyte. Also, in the PEO electrolyte with different combinations of Ag NPs and pure Zn NPs, the electrical conductivity increased as the pure Zn NPs concentration was higher.

3.2.2 Voltage-time transients during PEO experiments

To synthesis the antibacterial surface bearing Ag NPs and pure Zn NPs, the SLM implants were modified through PEO processing. The V-t transients were recorded during the process to observe the growth of the porous TiO₂ layer. The V-t curves (**Figure. 9**), demonstrated an initial voltage increase for 9 ± 1 seconds in all implant groups. After that, the V-t curves inflected, indicated the dielectric breakdown occurred with the presence of plasma discharge on the implant surface. The addition of Ag NPs and pure Zn NPs did not change the initial voltage rates (**Table. 3**), but slightly lower the breakdown voltage. Dielectric breakdown on PT implants was initiated at a voltage around 120.9 ± 2.9 V, while for PT-Zn and PT-Ag, the breakdown started at 116 ± 0.2 V and 109.8 ± 1.8 V, respectively. The addition of Ag NPs contributed to a significant lower breakdown voltage compared with Zn NPs. Furthermore, the voltage continued to increase linearly with a lower voltage rate of 0.25 V/s until the process ended at 300 seconds.

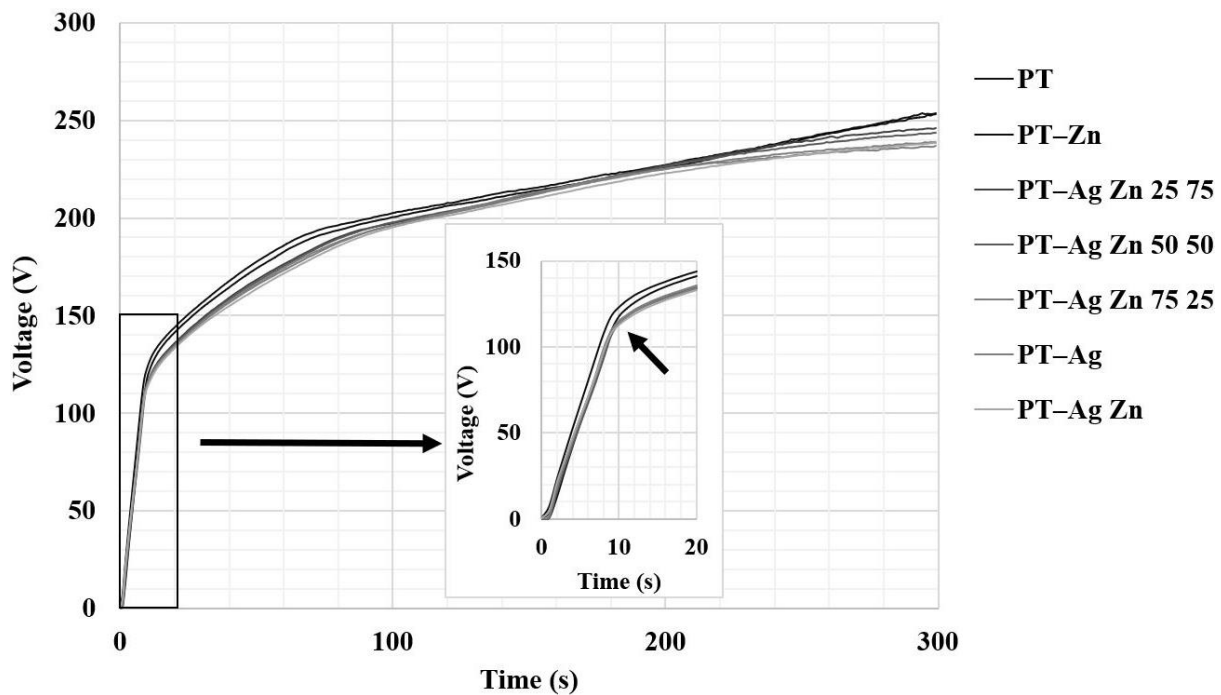


Figure. 9 The V-t curves recorded during PEO experiments. The black arrow indicates the dielectric breakdown.

Table. 3 Initial voltage rates, plasma discharging voltage, and final voltages in PEO experiments.

Experimental groups	Initial rate (V/s)	Dielectric breakdown voltage (V)	Final voltage (V)
PT	13.7 ± 1.2	120.9 ± 2.9	249.5 ± 1.3
PT-Zn	13.2 ± 0.3	116.0 ± 0.2	245.8 ± 2.7
PT-Ag Zn 25 75	13.1 ± 0.8	114.3 ± 1.3	241.6 ± 0.9
PT-Ag Zn 50 50	13.2 ± 0.8	113.1 ± 1.7	239.5 ± 2.4
PT-Ag Zn 75 25	12.9 ± 0.8	113.6 ± 1.9	237.5 ± 2.1
PT-Ag	13.1 ± 0.9	109.8 ± 1.8	232.5 ± 1.2
PT-Ag Zn	12.8 ± 1.3	113.1 ± 1.3	233.5 ± 2.1

3.3 Surface characteristics of biofunctionalized SLM implants

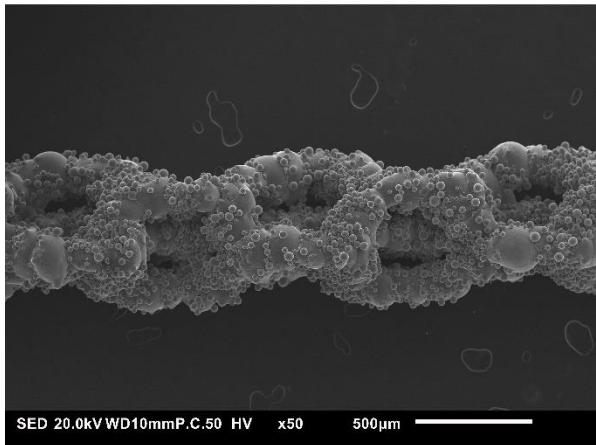
3.3.1 Surface morphology of biofunctionalized SLM implants

Surface morphology of the biofunctionalized SLM implants was analyzed using SEM imaging. Rough surface can be observed on the NT implants due to the partially melted Ti6Al4V particles on the surface (**Figure. 10A**). After the PEO processing, the PT implants were characterized by an interconnected micro/nano-porosity throughout the surface (**Figure. 10B**). Additional Ag NPs and pure Zn NPs in the PEO processing, PT-Ag Zn 50 50, did not change the surface morphology of the implants (**Figure. 10C**). All implants with Ag NPs and pure Zn NPs combinations displayed similar surface morphology (results not shown).

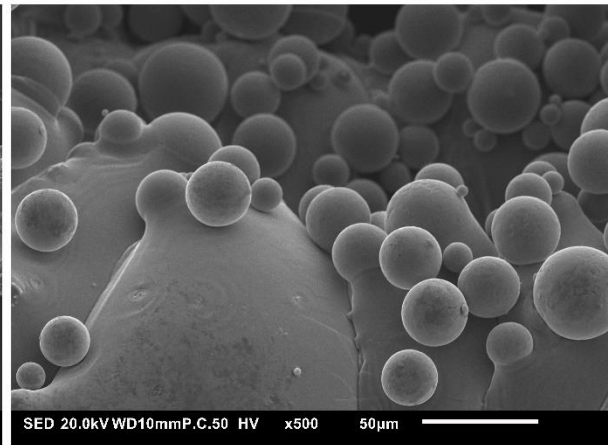
3.3.2 Distribution of Ag NPs and pure Zn NPs in TiO₂ surface

After PEO processing, Ag NPs and pure Zn NPs were found strongly attached to the biofunctionalized SLM implant surface. The adhered NPs on implant surface were confirmed by EDS spot analysis (**Figure. 11** and **12**), alongside with Ti, Al, and V from the implant substrate, as well as Ca and P from the electrolyte. Furthermore, PT-Ag Zn 25 75, PT-Ag Zn 50 50, and PT-Ag Zn 75 25 were compared using EDS surface analysis to observe the distribution of the NPs on the implant surface compared with the NPs concentrations added into PEO electrolyte. Results (**Figure. 13**) showed a significant difference in the NPs distributions on the implant surface, which determined the distinction among each implant group.

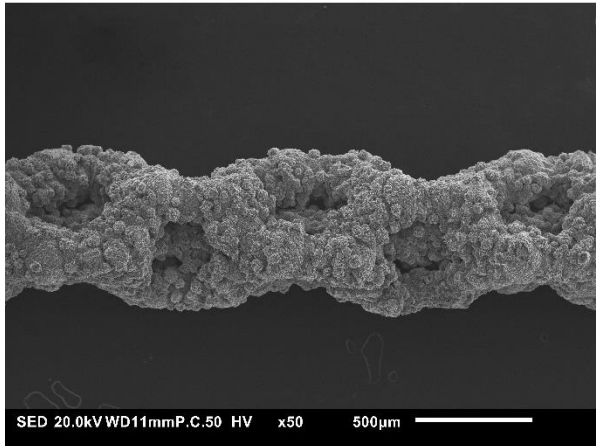
A. NT



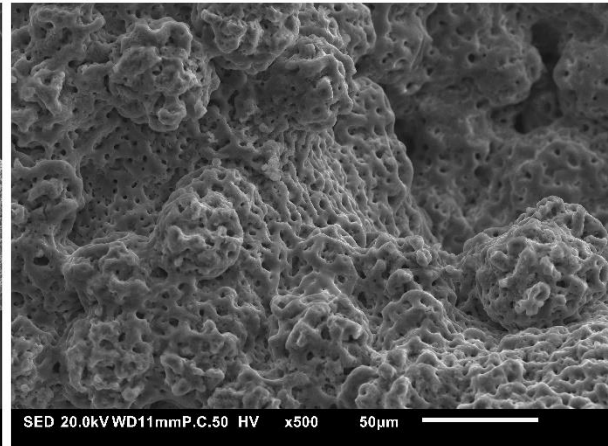
B.



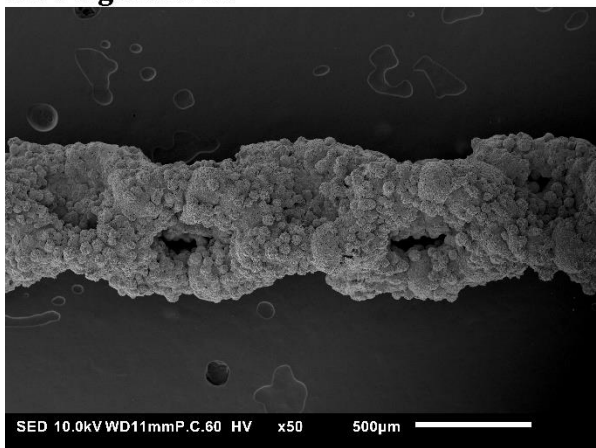
C. PT



D.



E. PT-Ag Zn 50 50



F.

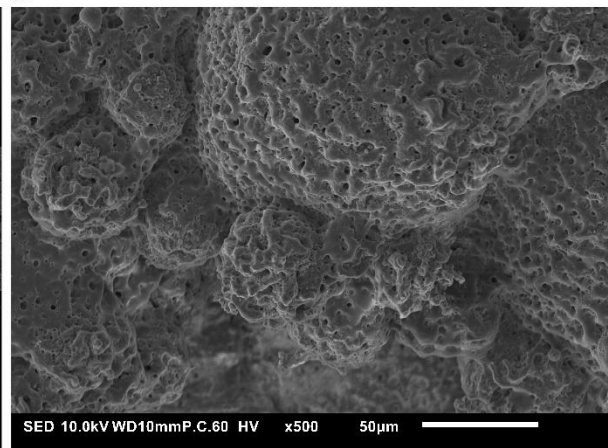
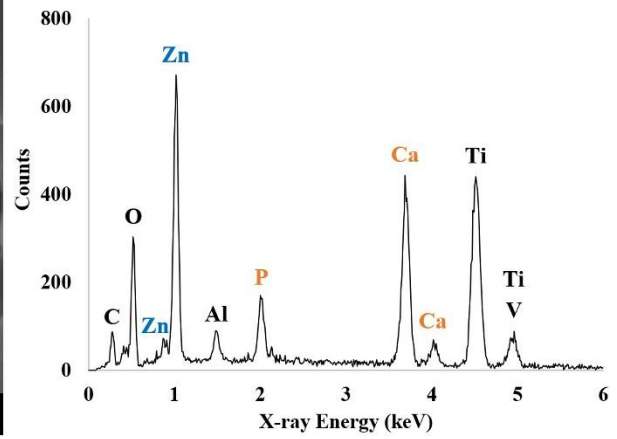
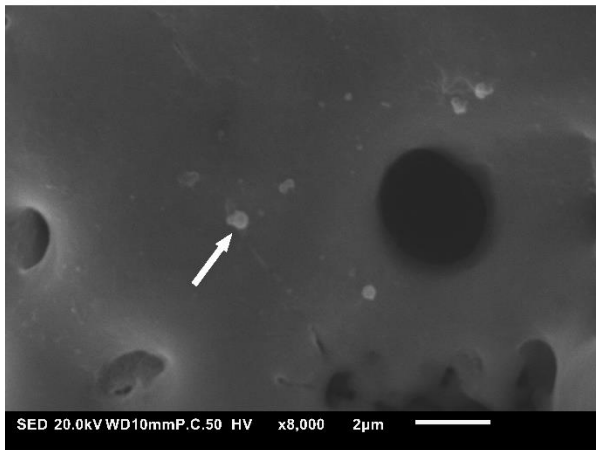
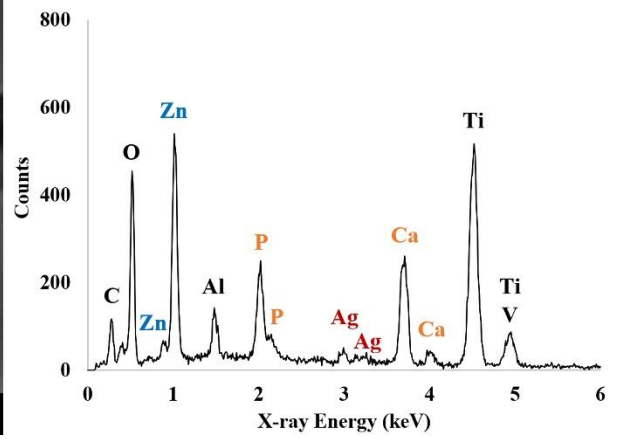
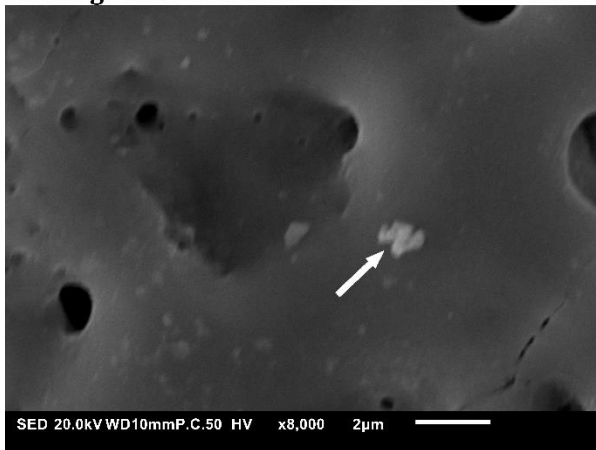


Figure. 10 Surface morphologies of SLM implants at 50× and 500× magnification. **A-B.** NT, **C-D.** PT, and **E-F.** PT-Ag Zn 50 50 implants.

A. PT-Zn



B. PT-Ag Zn 25 75



C. PT-Ag Zn 50 50

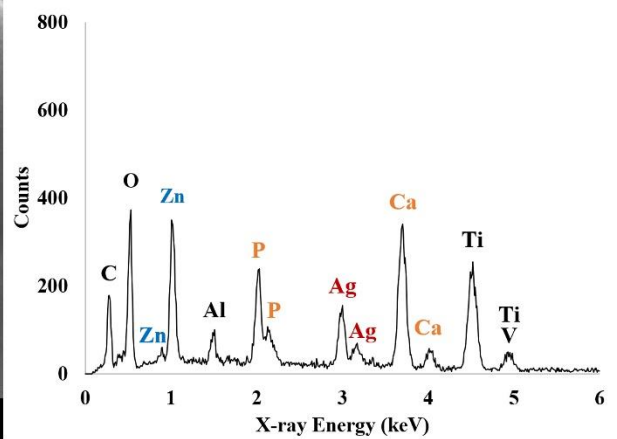
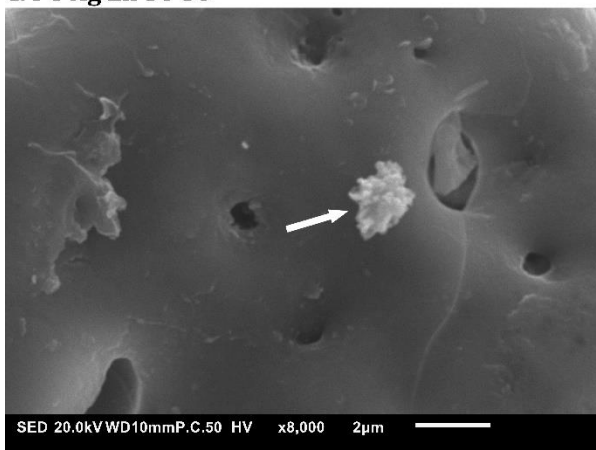
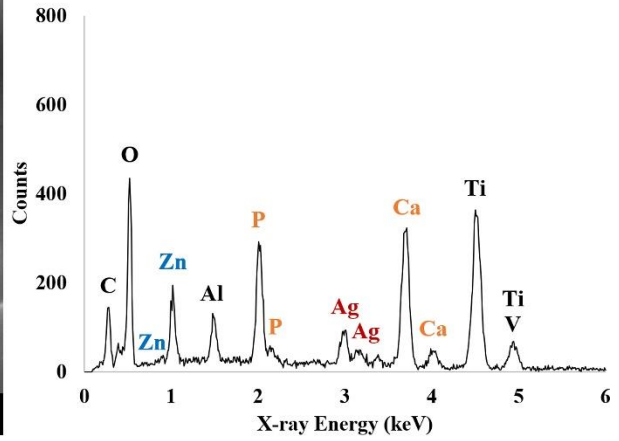
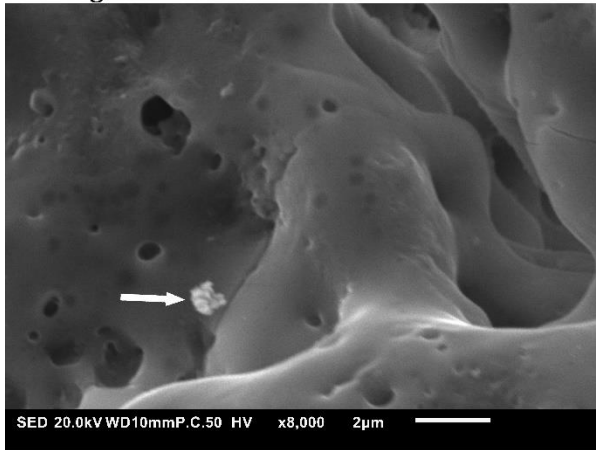
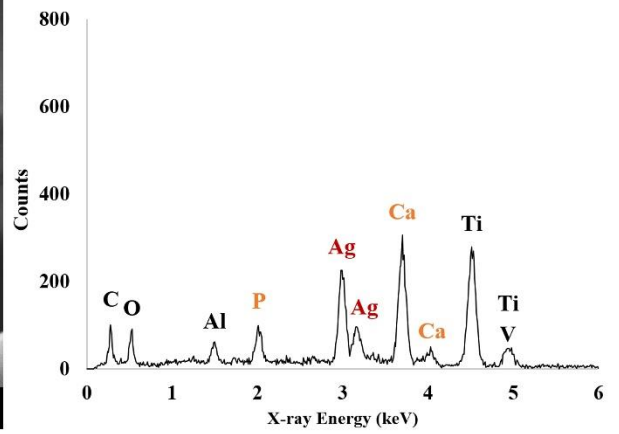
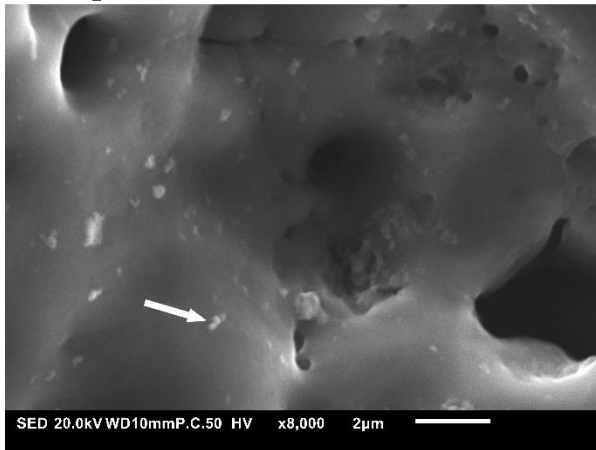


Figure. 11 EDS spot analysis of nanoparticles on **A.** PT-Zn, **B.** PT-Ag Zn 25 75, and **C.** PT-Ag Zn 50 50 implants surfaces.

A. PT-Ag Zn 75 25



B. PT-Ag



C. PT-Ag Zn

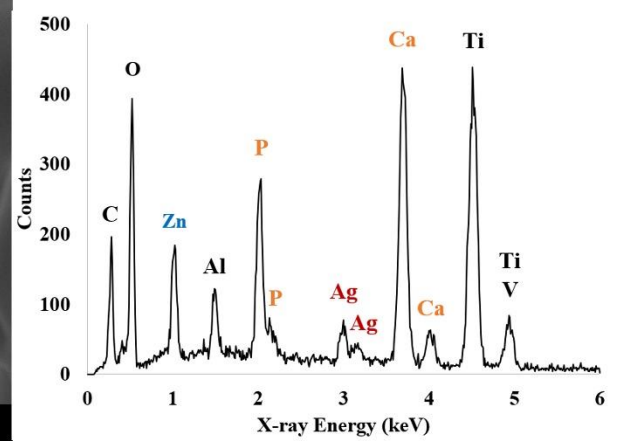
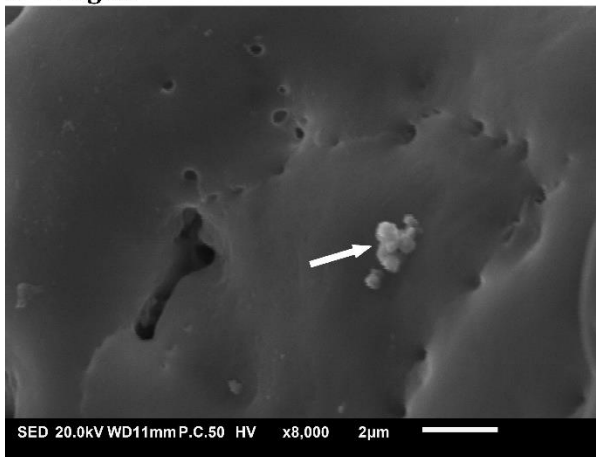


Figure. 12 EDS spot analysis of nanoparticles on **A.** PT-Ag Zn 75 25, **B.** PT-Ag, and **C.** PT-Ag Zn implants surfaces.

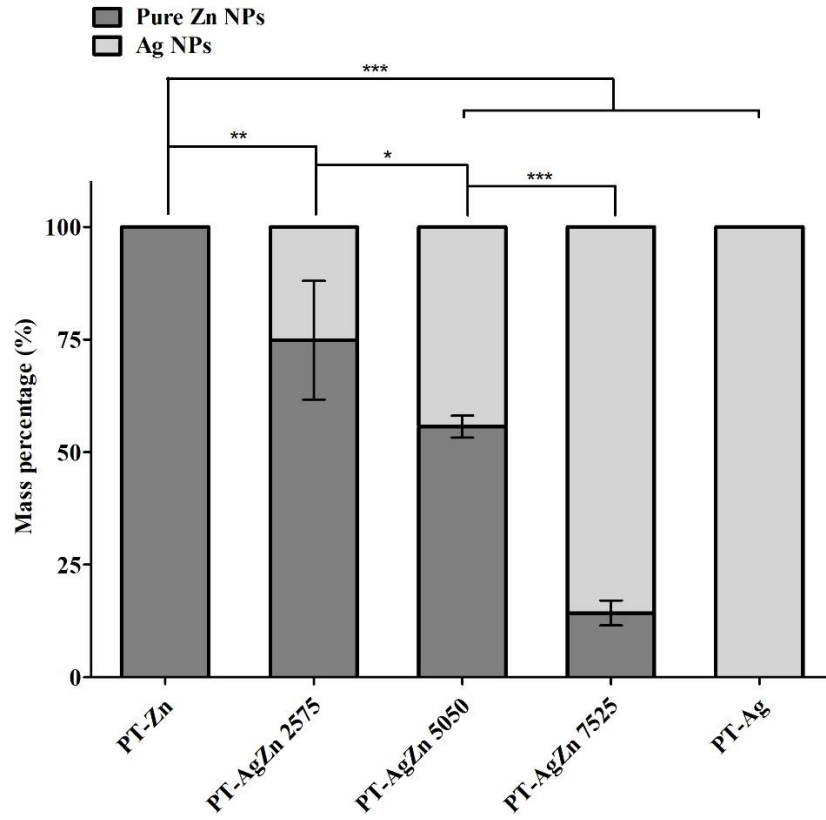
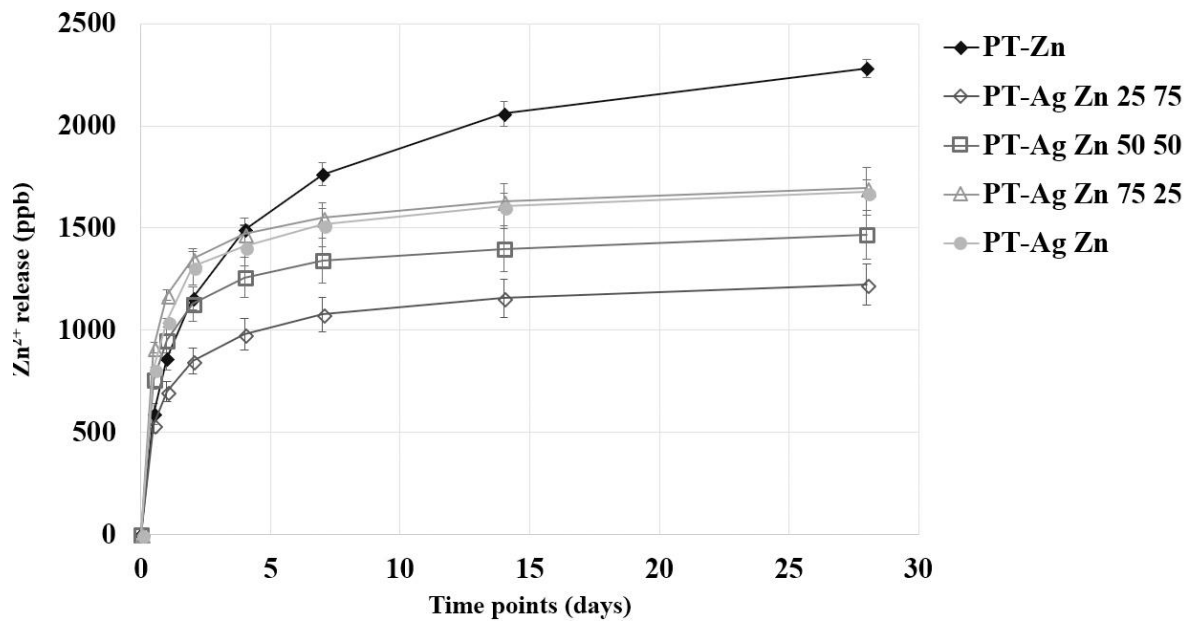


Figure. 13 Ratio of Ag NPs and pure Zn NPs on the implant surface.

3.4 Ag⁺ and Zn²⁺ ion release kinetics

To investigate the relationship between Ag NPs and pure Zn NPs on the biofunctionalized SLM implants surface, Ag⁺ and Zn²⁺ ion release concentrations were measured by ICP-OES. The initial burst release of Ag⁺ and Zn²⁺ ions was observed in the first 12 hours, followed by a progressive slower ion release up to 28 days (Figure. 14).

A. Cumulative Zn²⁺ release



B. Cumulative Ag⁺ release

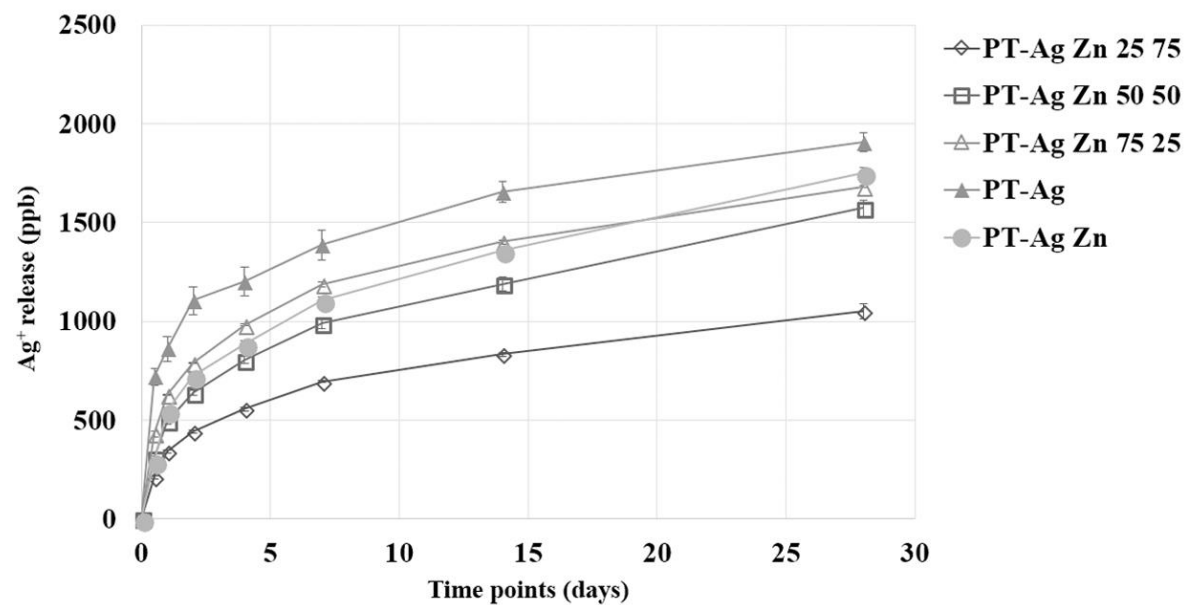


Figure. 14 Cumulative release kinetics of A. Zn²⁺ and B. Ag⁺ ions from the biofunctionalized SLM implants.

Accumulatively, the Ag⁺ and Zn²⁺ ion release concentration increased along with the extended immersion time. The highest Ag⁺ ion concentration was released by PT–Ag (1906.2 ppb), followed by PT–Ag Zn (1749.7 ppb), PT–Ag Zn 75 25 (1681.9 ppb), PT–Ag Zn 50 50 (1573.5 ppb), and PT–Ag Zn 25 75 (1052.4 ppb), respectively. While the highest Zn²⁺ ion concentration was produced by PT–Zn (2281.3 ppb), followed by PT–Ag Zn 75 25 (1697 ppb), PT–Ag Zn (1678.6 ppb), PT–Ag Zn 50 50 (1467.5 ppb), and PT–Ag Zn 25 75 (1223.7 ppb), respectively.

The ion release kinetics, on the implants with Ag NPs and pure Zn NPs combinations, demonstrated a high Zn²⁺ ions release in the early hours, while the release of Ag⁺ ions increased at latter time points. As shown by the non-cumulative ion release (**Figure. 15**), the initial 12 hours Zn²⁺ ion release concentration from PT–Ag Zn 50 50 (757.27 ppb), PT–Ag Zn 75 25 (913.23 ppb), and PT–Ag Zn (810.36 ppb) were higher when compared with PT–Zn (588.88 ppb). On the other hand, the 12 hours Ag⁺ ion release concentration from PT–Ag Zn (293.55 ppb) was lower than PT–Ag (720.69 ppb). Also, slightly lower Ag⁺ ion concentrations were released from PT–Ag Zn 50 50 and PT–Ag Zn 75 25 when compared with the implants containing same amount of Ag NPs (results not shown). This ion release kinetics demonstrated a dominant Zn²⁺ ion release in the early time point, consequently, the Zn²⁺ ion release concentrations were much lower in the following days. While, the slower initial release of Ag⁺ ion resulted in an increasing ion release concentration at latter time points.

Furthermore, EDS analysis (**Figure. 16**) was performed for PT–Ag Zn 25 75, PT–Ag Zn 50 50, PT–Ag Zn 75 25, and PT–Ag Zn after 24 hours ion release. The results demonstrated a lower pure Zn NPs concentration on the implant surfaces compared with Ag NPs, which were resulted from a higher initial burst of Zn²⁺ ions than Ag⁺ ions from the implant surface. The cumulative Ag⁺ and Zn²⁺ ion release concentrations after 24 hours (**Table. 4**), indicated that the preferential release of Zn²⁺ ions and slower release of Ag⁺ ions occurred only in PT–Ag Zn 50 50, PT–Ag Zn 75 25, and PT–Ag Zn.

Table. 4 Cumulative Ag⁺ and Zn²⁺ ion release concentrations from biofunctionalized SLM implants.

Experimental groups	Ag ⁺ ion release (ppb)	Zn ²⁺ ion release (ppb)
PT–Zn	–	861.4
PT–Ag Zn 25 75	343.9	697.9
PT–Ag Zn 50 50	495.4	951.7
PT–Ag Zn 75 25	630.6	1242.3
PT–Ag	860.5	–
PT–Ag Zn	549.2	1309.9

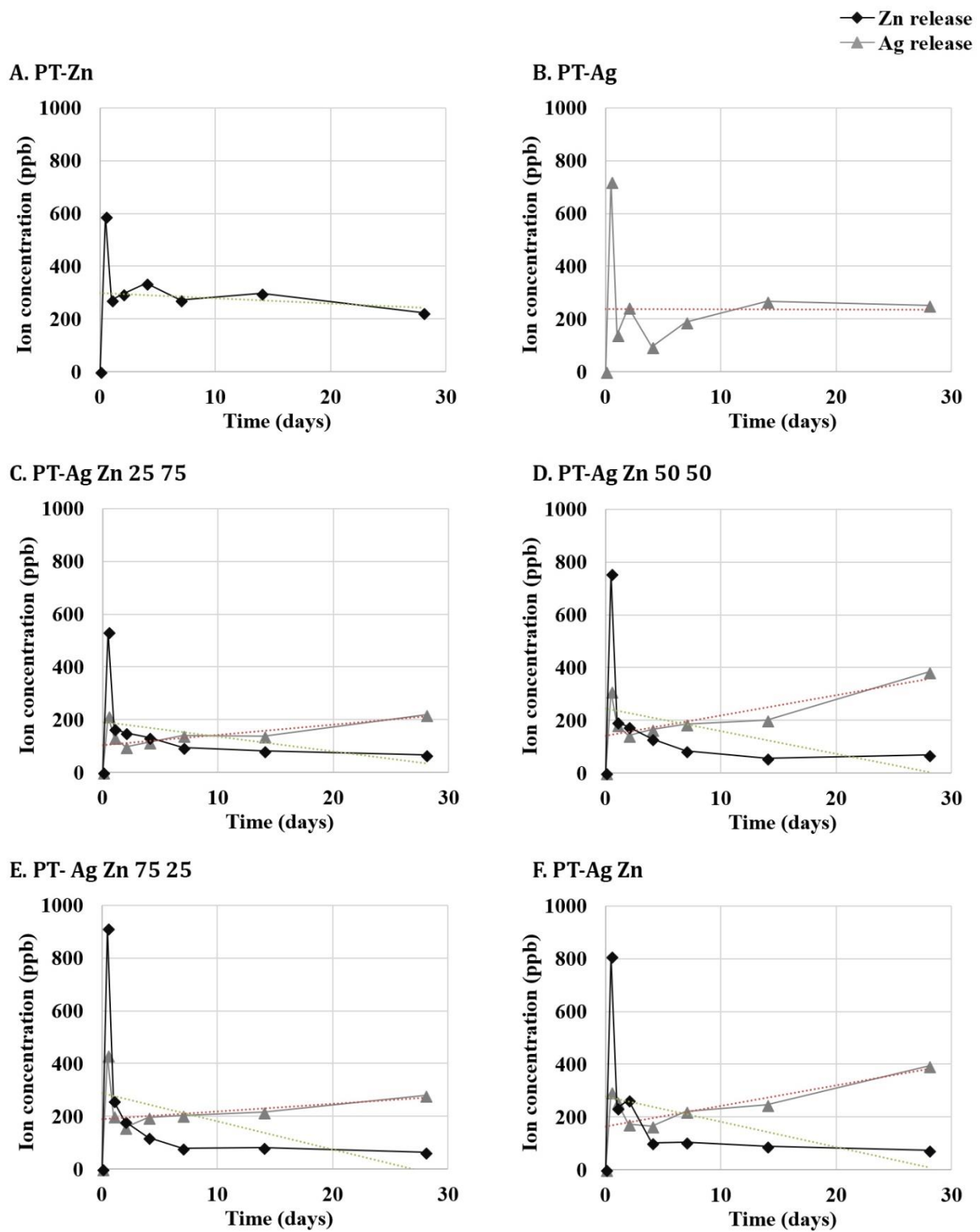


Figure. 15 Non-cumulative Zn^{2+} and Ag^+ ion release interaction from the biofunctionalized SLM implant. **A.** PT-Zn, **B.** PT-Ag, **C.** PT-Ag Zn 25 75, **D.** PT-Ag Zn 50 50, **E.** PT-Ag Zn 75 25, and **F.** PT-Ag Zn

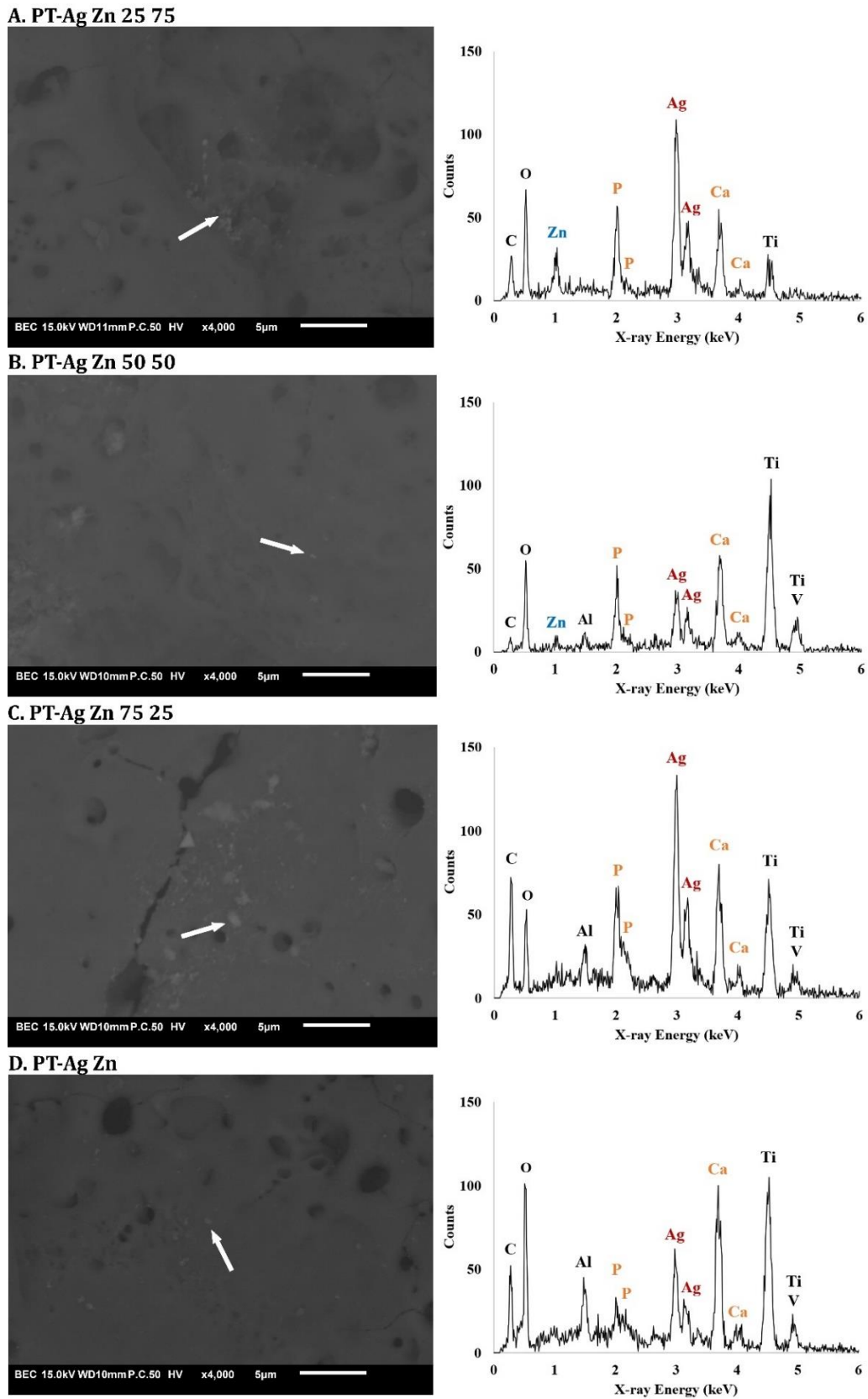


Figure. 16 EDS spot analysis of nanoparticles on **A.** PT–Ag Zn 25 75, **B.** PT –Ag Zn 50 50, **C.** PT–Ag Zn 75 25 and **D.** PT–Ag Zn implants surfaces, after 24 hours ion release. Data representative for 5 spots per group.

3.5 Hydroxyl radical generation

The $\cdot\text{OH}$ radical generation was detected by EPR spectrometer, involving DMPO spin trapping agent in PBS solution. The EPR results (**Figure. 17**) demonstrated DMPO–OH spectra from PT, PT–Zn, PT–Ag Zn 25 75, PT–Ag Zn 50 50, PT–Ag Zn 75 25, PT–Ag and PT–Ag Zn, which indicated the presence of $\cdot\text{OH}$ radical generated from the biofunctionalized SLM implant surface. While, no radical generation was observed in NT implants. The DMPO–OH spectrum was characterized by the presence of four lines signal with 1:2:2:1 intensity, g value of 2.0042, and hyperfine splitting parameters of $a^{\text{N}} = 15$, $a^{\text{H}} = 15$. Besides DMPO–OH spectra, DMPO–CH₃ were also detected only in PT, PT–Zn, and PT–Ag implants in the first 10 minutes. The DMPO–CH₃ spectrum was characterized by six lines signal with equal intensity of each lines, g value of 2.0045, and hyperfine splitting parameters of $a^{\text{N}} = 15.41$, $a^{\text{H}} = 23.5$ [39].

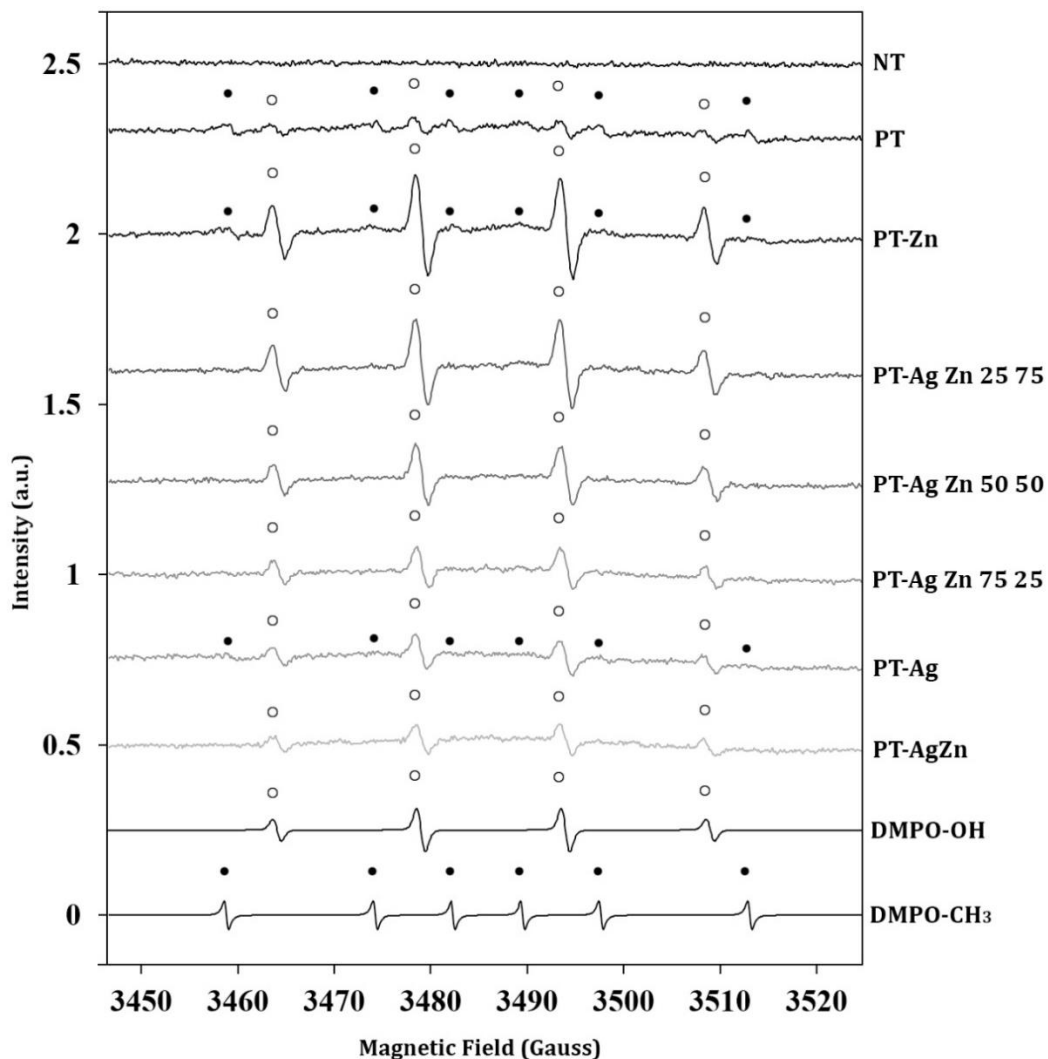


Figure. 17 DMPO–OH and DMPO–CH₃ radicals spectra generated from all SLM implant groups.

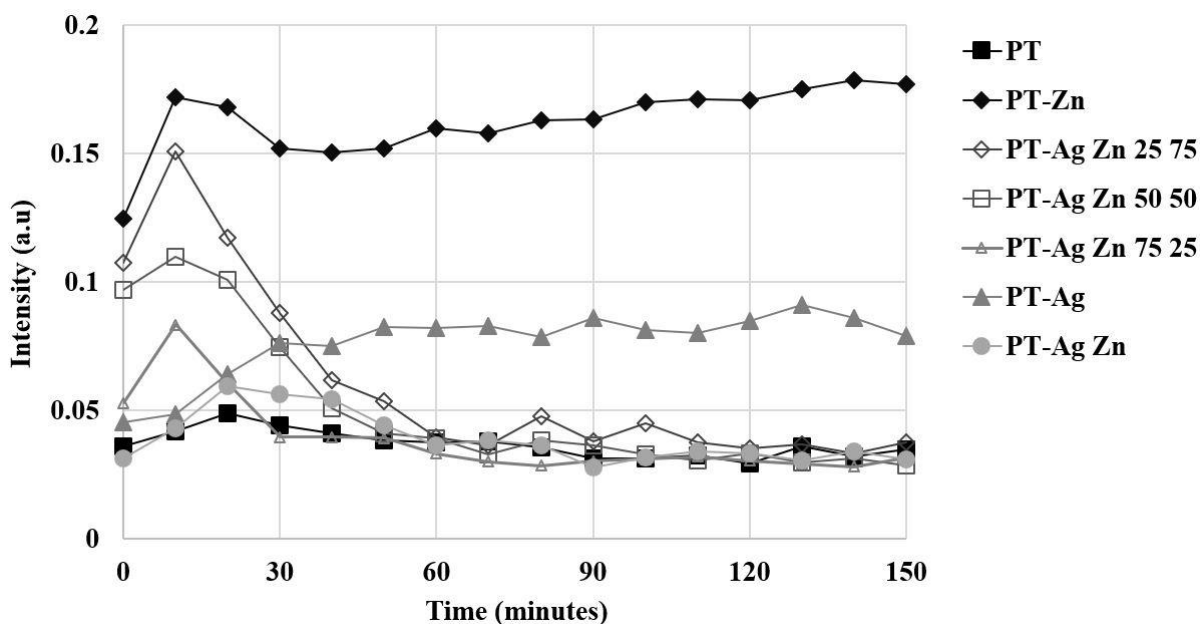


Figure. 18 $\cdot\text{OH}$ radical intensity generated by biofunctionalized SLM implants submerged in 20 mM DMPO–PBS solution over 150 minutes.

The $\cdot\text{OH}$ radicals measurements results showed that PT–Zn established the highest $\cdot\text{OH}$ radical intensity, **Figure. 18**, which was about two times higher than PT–Ag, and approximately four times higher than PT implant. The $\cdot\text{OH}$ radical intensity was increasing over time from PT–Zn and PT–Ag implants. While, in PT–Ag Zn 25 75, PT–Ag Zn 50 50, PT–Ag Zn 75 25, and PT–Ag Zn implants, the $\cdot\text{OH}$ radical intensity was only increased in the first 20 minutes, and significantly dropped afterwards. The immediate $\cdot\text{OH}$ radical generations, within 10 minutes after the DMPO–PBS solution was added, demonstrated the highest $\cdot\text{OH}$ radical intensity was generated by PT–Zn (0.17 a.u.) and followed by PT–Ag Zn 25 75 (0.15 a.u.), PT–Ag Zn 50 50 (0.11 a.u.), PT–Ag Zn 75 25 (0.08 a.u.), and PT–Ag (0.05 a.u.), whereas PT – Ag Zn reached the highest $\cdot\text{OH}$ radical intensity, 0.06 a.u., at the 20 minutes after DMPO–PBS solution was added. The results clearly demonstrated that the inclusion of pure Zn NPs contributed more to the $\cdot\text{OH}$ radical generation than Ag NPs.

3.6 *In vitro* antibacterial activity of SLM implants

3.6.1 Inhibition zones

The leaching activity of biofunctionalized SLM implants with Ag NPs and pure Zn NPs was assessed against MRSA USA300 in the LB-agar plates. After 24 hours of incubation, the agar plates displayed zones of inhibition for all implants with NPs, except for PT–Zn implants. Also, no inhibition zones were observed for the NT and PT implants, **Figure. 19**. The inhibition zones demonstrated comparable inhibition zones among PT–Ag Zn 25 75, PT–Ag Zn 50 50, PT–Ag Zn 75 25, PT–Ag Zn, and PT–Ag implants. The results implied that substituting partly of Ag NPs content with pure Zn NPs does not reduce the antibacterial leaching activity of the implants.

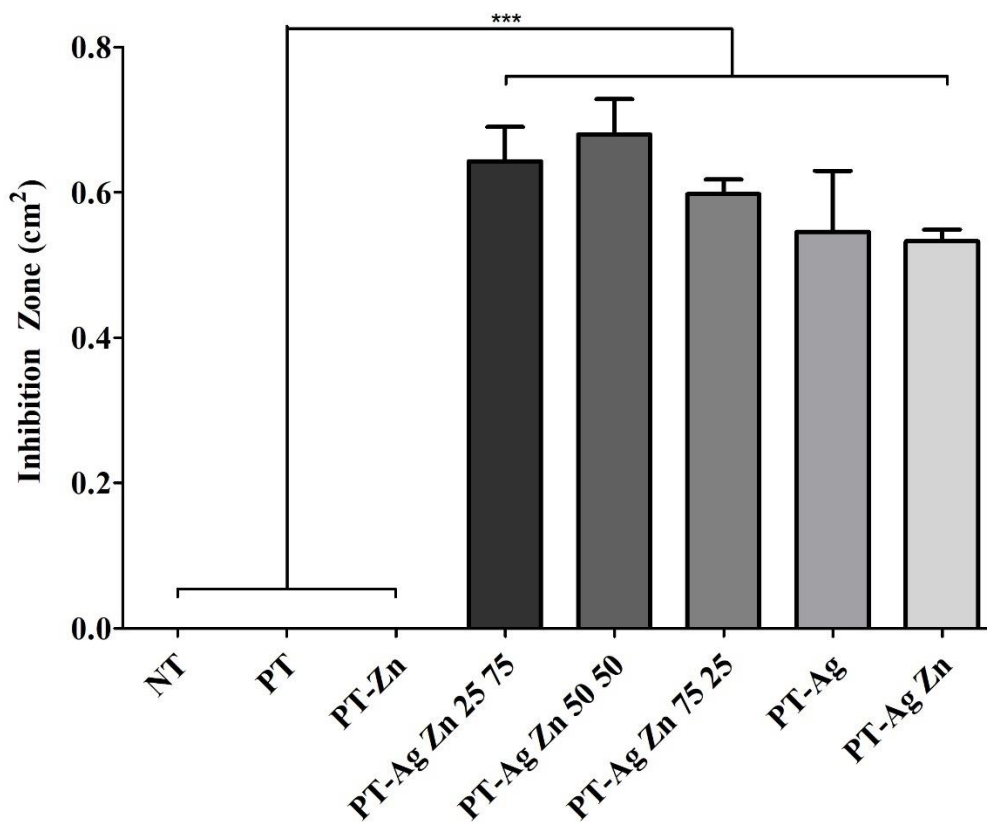
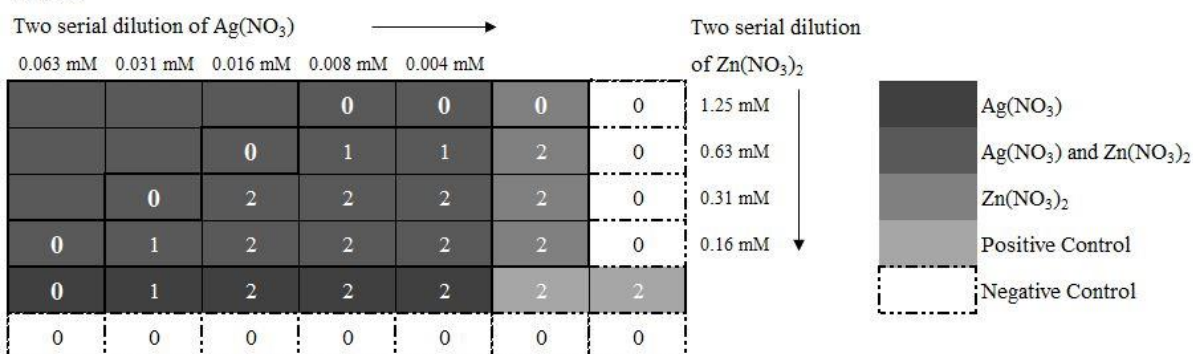


Figure. 19 Inhibition zones from biofunctionalized SLM implants against MRSA USA300 on LB-agar plate. n=3 per group. *** p<0.001.

3.6.2 Minimum inhibitory and bactericidal concentration of AgNO₃ and Zn(NO₃)₂

The MIC and MBC of Ag⁺ and Zn²⁺ ions were determined by testing various concentrations of AgNO₃ and Zn(NO₃)₂ against MRSA USA300. The results demonstrated that Ag⁺ ions had a stronger antibacterial activity compared to Zn²⁺ ions. After 24 hours of incubation, the MIC was 0.063 mM for AgNO₃ and 1.25 mM Zn(NO₃)₂, while, the MBC was 0.25 mM for AgNO₃ and 10 mM for Zn(NO₃)₂. Combinations of AgNO₃ and Zn(NO₃)₂ demonstrated a synergistic potential where the inhibitory and bactericidal activity were achieved at a lower concentration from both ions (**Figure. 20**).

A. MIC



B. MBC

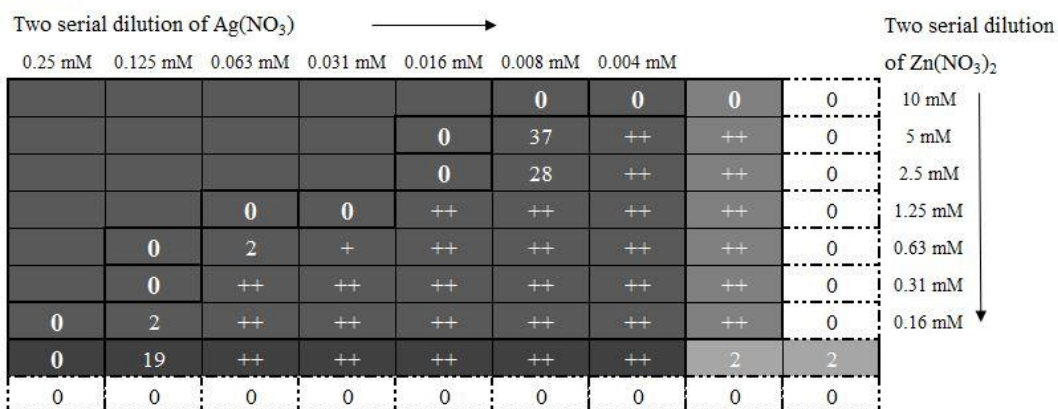


Figure. 20 **A.** MIC of AgNO₃, Zn(NO₃)₂, and the combinations against MRSA USA300. 0, 1, and 2 represents no visual turbidity, small, and large turbidity observed. **B.** MBC of AgNO₃, Zn(NO₃)₂, and the combinations against MRSA USA300. Number of countable bacterial colonies are presented in the table, while 0 and ++ indicate no bacterial colonies and plenty of bacteria colonies, respectively.

3.6.3 Bactericidal activity against adherent and non-adherent MRSA

The antibacterial properties of biofunctionalized SLM implants were evaluated by incubating the implants into 100 μ L of 10^2 CFU MRSA USA300. After overnight incubation, the bactericidal activities against adherent bacteria (**Figure. 21**) were observed on PT–Ag implants and all implant groups with Ag NPs and pure Zn NPs combinations. While the bactericidal properties against non-adherent bacteria (**Figure. 22**) were shown only by PT–Ag Zn 75 25, PT–Ag, and PT–Ag Zn. The results showed that PT–Ag Zn 75 25 demonstrated a stronger antibacterial activity compared with PT–Ag Zn 50 50 and PT–Ag Zn 25 75. There were no antibacterial properties observed in PT–Zn, instead a slightly increase number of adherent bacteria were quantified from the implant compared with NT and PT implants. The results suggested that the substitution of Ag NPs with pure Zn NPs can prevent MRSA adhesion on implant surface and reduce the number of non-adherent bacteria.

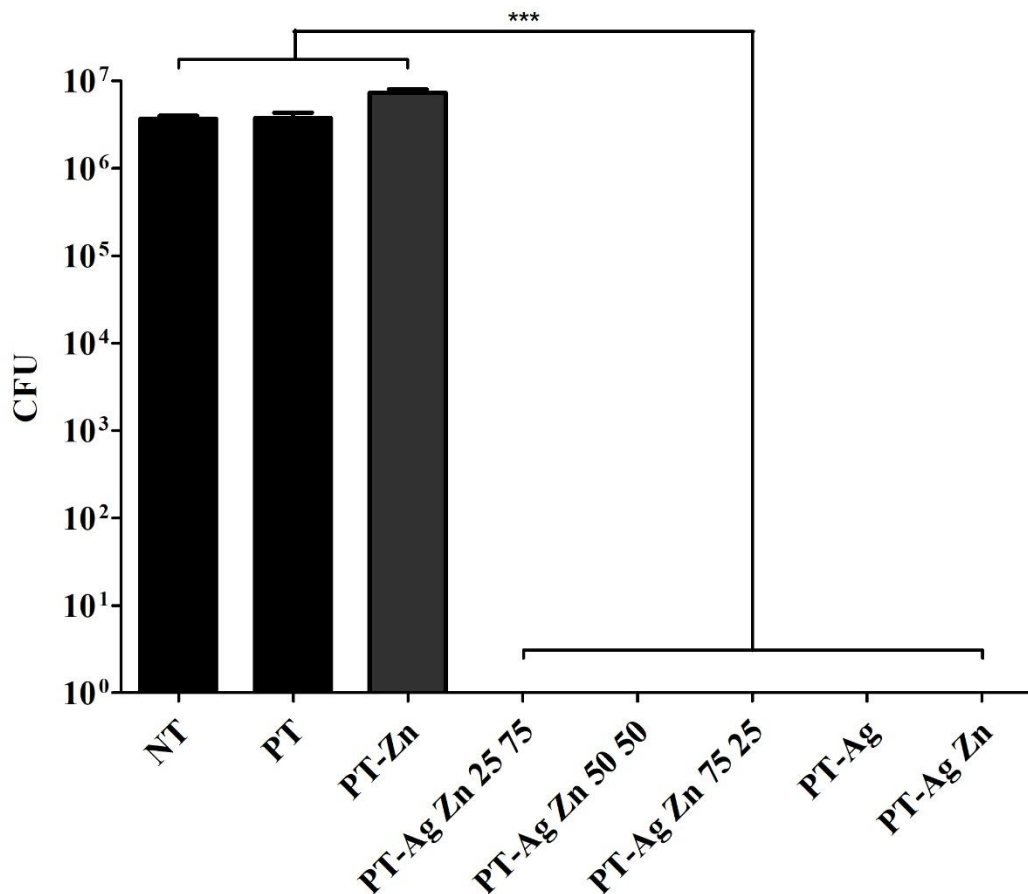


Figure. 21 Bactericidal activity of biofunctionalized SLM implants against adherent MRSA USA300, after overnight incubation with 10^2 CFU MRSA. n=3 per group. *** p<0.001.

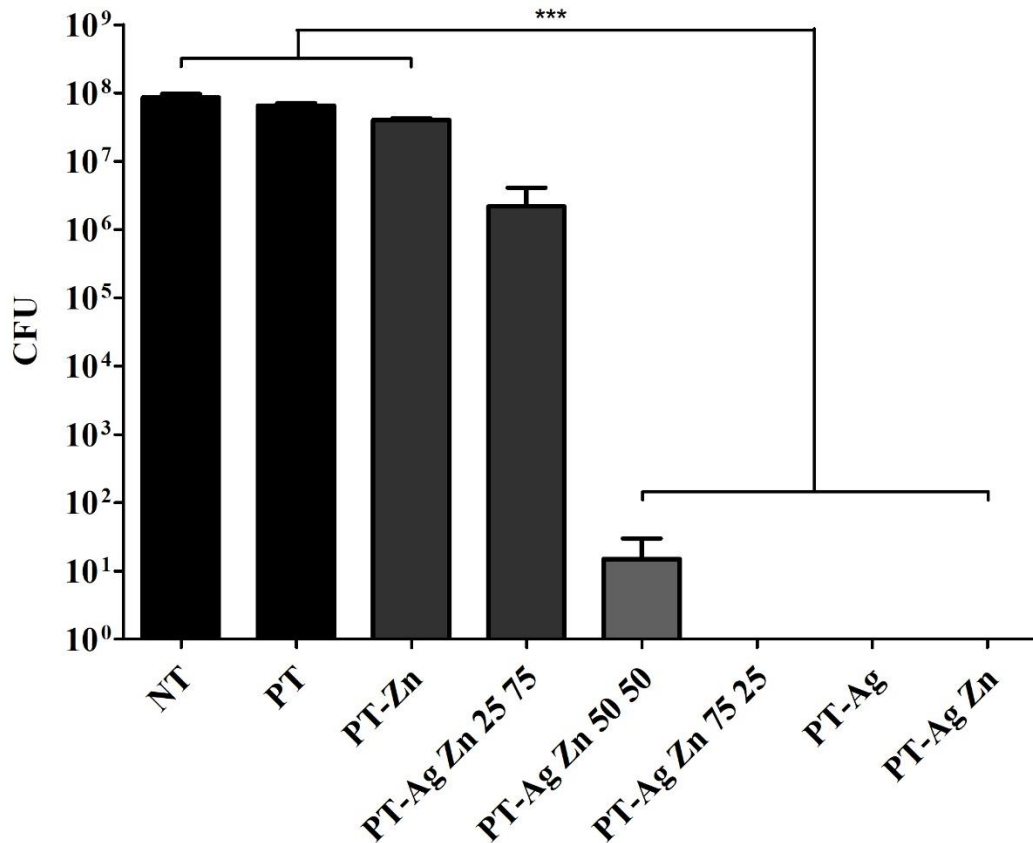


Figure. 22 Bactericidal activity of biofunctionalized SLM implants against non-adherent MRSA USA300, after overnight incubation with 10^2 CFU MRSA. n=3 per group. *** p<0.001.

3.6.4 Anti-biofilm activity

MRSA USA300 biofilm formation was assessed by incubating the biofunctionalized SLM implants in TSB medium containing 200 MRSA CFU with additional 1% glucose for 24 hours. The results demonstrated biofilm initiations only on NT implant surface (**Figure. 23A-B**). While, hundreds to thousands bacterial adhesions covered a substantial surface of PT (**Figure. 23C-D**), and PT-Zn implant, (**Figure. 23E-F**). A reduction of bacterial adhesions was observed on PT-Ag Zn 25 75, PT-Ag Zn 50 50, and PT-Ag Zn 75 25 implants (**Figure. 24**), as well as in PT-Ag and PT-Ag Zn implants (**Figure. 25**), with only few dozens of bacteria colonies were found, attached in the deep porous area of the implants surface. Overall, the biofunctionalized SLM implants, which contained only Ag NPs and the combinations of Ag NPs and pure Zn NPs on the surface, prevented biofilm formations for 24 hours.

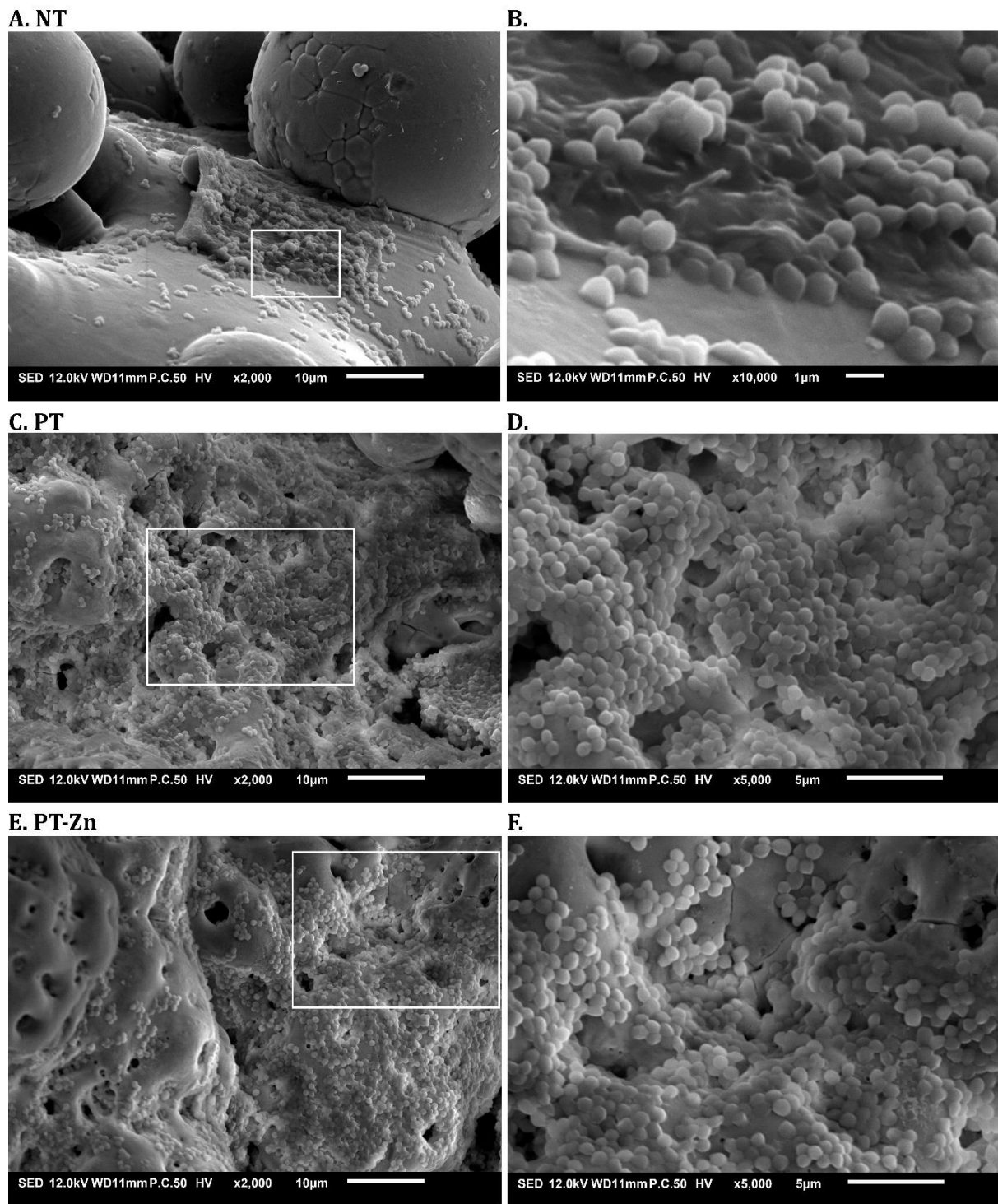
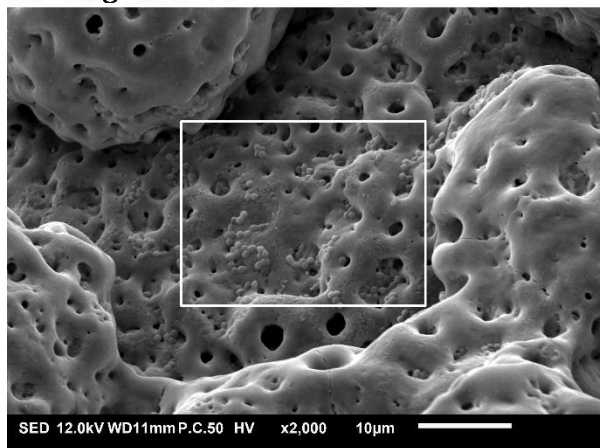
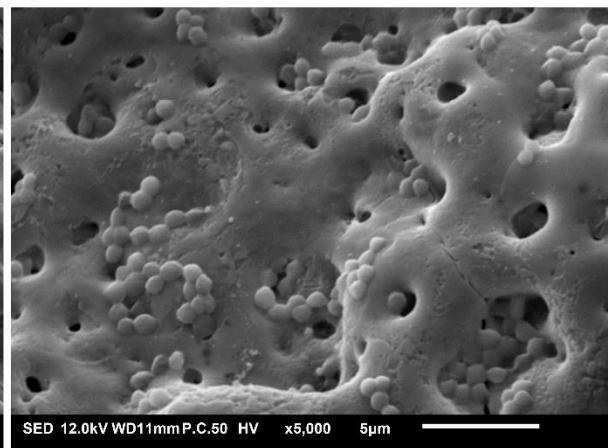


Figure. 23 SEM images of MRSA USA300 biofilm formations on SLM implants after 24 hours incubation in TSB 1% glucose, 2000× and 5000× / 10,000× magnification. **A-B.** NT, **C-D.** PT, and **E-F.** PT-Zn. Image representative for n=3 per group.

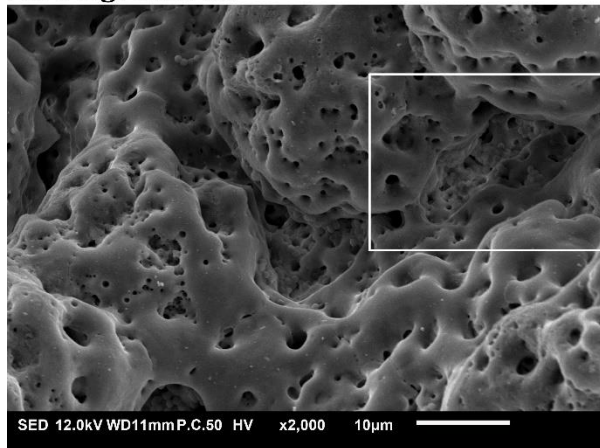
A. PT-Ag Zn 25 75



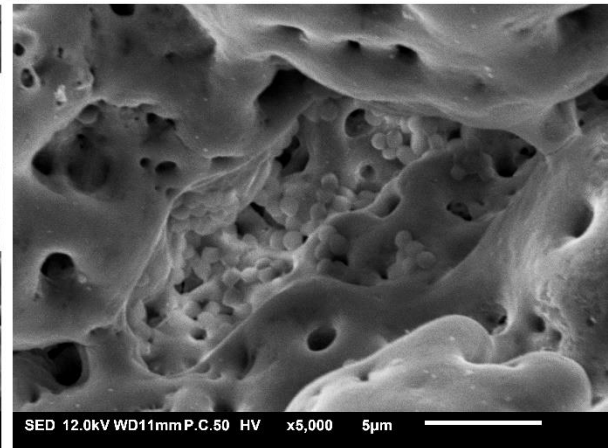
B.



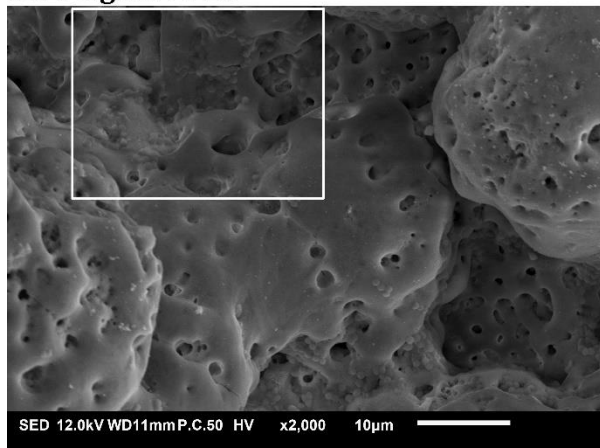
C. PT-Ag Zn 50 50



D.



E. PT-Ag Zn 75 25



F.

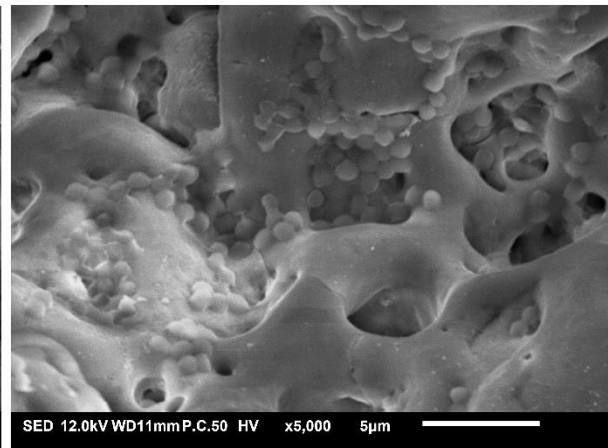
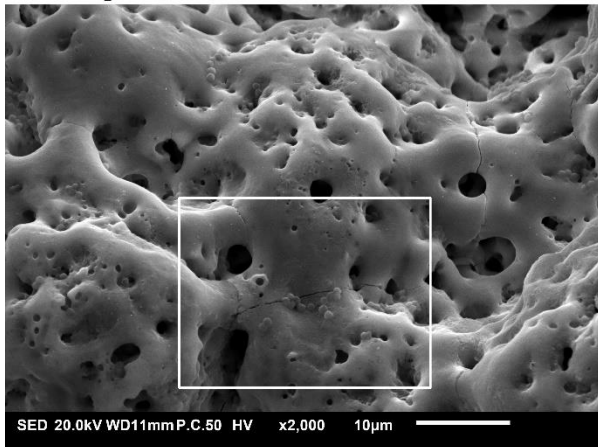
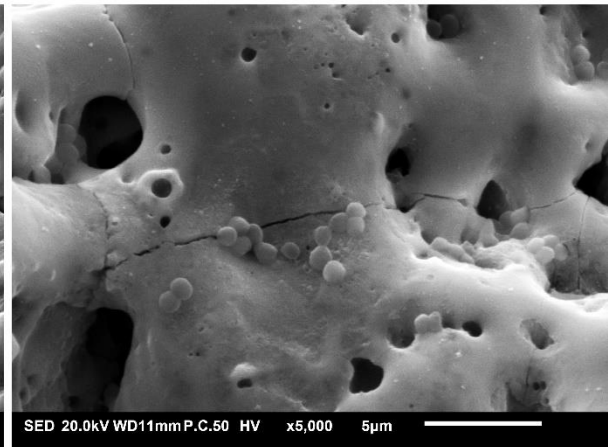


Figure. 24 SEM images of MRSA USA300 biofilm formations on SLM implants after 24 hours incubation in TSB 1% glucose, 2000 \times and 5000 \times magnification. **A-B.** PT-Ag Zn 25 75, **C-D.** PT-Ag Zn 50 50, and **E-F.** PT-Ag Zn 75 25. Image representative for n=3 per group.

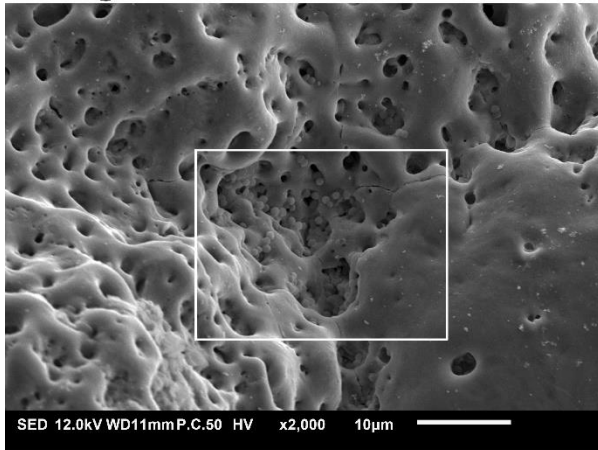
A. PT-Ag



B.



C. PT-Ag Zn



D.

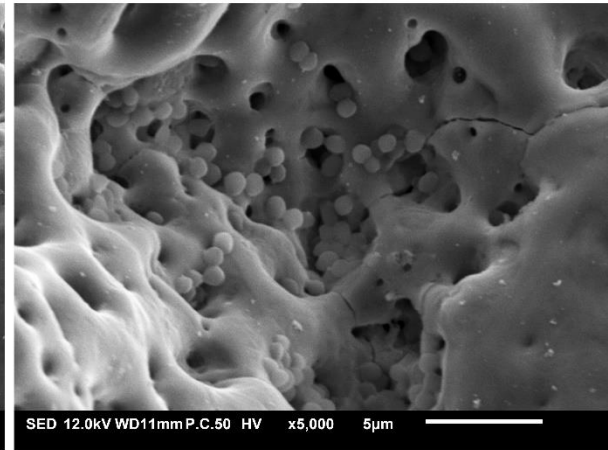


Figure. 25 SEM images of MRSA USA300 biofilm formations on SLM implants after 24 hours incubation in TSB 1% glucose, 2000× and 5000× magnification. **A-B.** PT–Ag and **C-D.** PT–Ag Zn. Image representative for n=3 per group.

4 Discussion

4.1. Discussion of the results

This study aimed to synthesize antibacterial SLM Ti6Al4V implants bearing Ag NPs and pure Zn NPs. Porous implants were designed and fabricated through SLM additive manufacturing process. Subsequently, the implants surface was modified by PEO processing to integrate Ag NPs and pure Zn NPs on the converted interconnected nano/microporous TiO₂ surface. Biomaterial characterizations were performed to observe the surface morphology, chemical compositions, the release kinetics of Ag⁺ and Zn²⁺ ions, as well as the ·OH radical generation. Lastly, *in vitro* antibacterial experiments against MRSA USA300 were conducted to assess the antibacterial properties of the SLM implants.

Before PEO processing, the morphology and phase composition of Ag NPs and pure Zn NPs were observed using SEM and XRD analysis (**Figure. 5** and **6**). The as-purchased colloidal Ag NPs had irregular shapes with a wide XRD spectrum, while pure Zn NPs were in spherical shape with a sharp XRD peaks. The wide XRD spectrum on the colloidal Ag NPs indicates the presence of the amorphous materials binding the Ag NPs [40]. Moreover, the stability of Ag NPs and pure Zn NPs in the PEO electrolyte was characterized by zeta potential and hydrodynamic size distribution measurements. The magnitude of zeta potential is an indicator of the NPs dispersibility in a suspension [38]. A high zeta potential (± 30 mV) means that the NPs are stable, well-dispersed, and should result in a small (non-agglomerated) particle size. In the PEO electrolyte, adsorption of ions on the Ag NPs and pure Zn NPs creates an electrical double layer (**Figure. 26A**), which results in an electrostatic repulsion between the NPs and is measured as the zeta potential [41]. Results (**Figure. 7**) indicated that Ag NPs had a higher zeta potential than pure Zn NPs in PEO electrolyte, meaning that Ag NPs should have a smaller size than pure Zn NPs. In contrast, the hydrodynamic size distribution showed that Ag NPs formed a larger particle size than pure Zn NPs (**Figure. 8**).

According to the Derjaguin Landau Verwey and Overbeek (DLVO) colloidal stability theory, a stable NPs dispersion is based on the total forces of the electrostatic repulsion and the van der Waals attraction [41]. Meanwhile, zeta potential only determines the electrostatic repulsion without taking the van der Waals attraction into consideration [42]. In PEO electrolyte, Ag NPs carried a certain repulsion force that was higher than pure Zn NPs. However, due to a stronger van der Waals attraction, the net forces drove the Ag NPs to form weak flocculants (**Figure. 26B**) that resulted in a large hydrodynamic particle size. In comparison, pure Zn NPs had a smaller hydrodynamic particle size than Ag NPs (**Figure. 26C**), which could be a result of the van der Waals attraction not being strong

enough to exceed the electrostatic repulsion force. Since van der Waals forces are inevitable during the hydrodynamic size measurements, it is not unusual to discover a stable zeta potential value with a large hydrodynamic particle size or vice versa [43]. Nonetheless, the weak flocculants formed in the electrolyte can be re-dispersed through mechanical agitation such as stirring or ultrasonication during PEO processing.

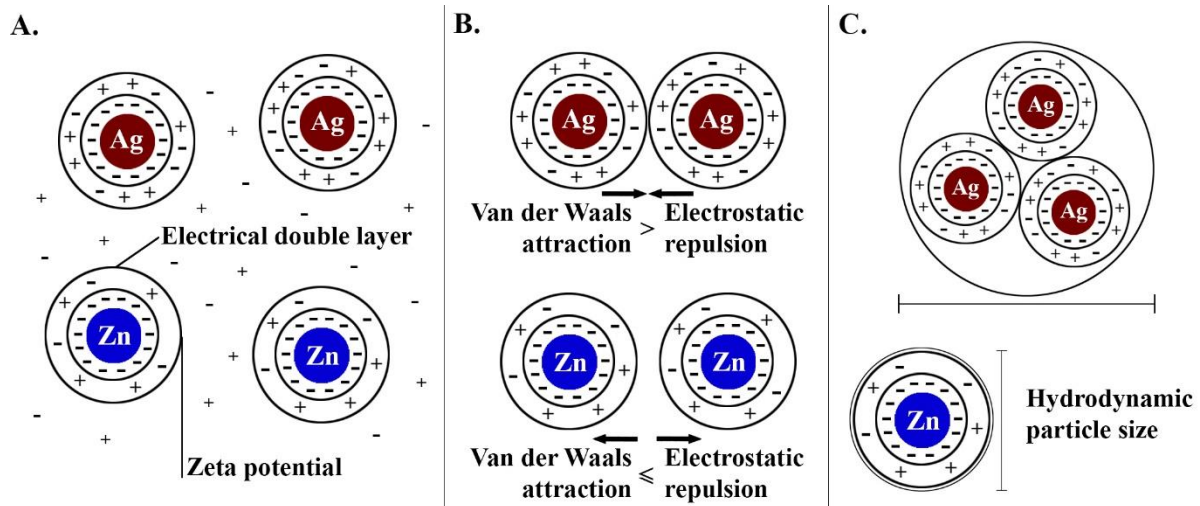


Figure. 26 Illustration of Ag and pure Zn nanoparticles stability in PEO electrolyte. **A.** Ag and pure Zn nanoparticles interact with the surrounding ions. **B.** The net forces of electrostatic repulsion and van der Waals attraction that determine the stability of the nanoparticles in the electrolyte. **C.** The hydrodynamic particle size for Ag and pure Zn nanoparticles.

In addition to the stability of Ag NPs and pure Zn NPs in the PEO electrolyte, the electrical conductivity of the electrolyte was also measured before PEO processing. Electrical conductivity of the electrolyte is important as it influences the discharge characteristics and coating formation through its ability in letting the electrical charges flow during PEO process. Conductivity of the electrolyte for PEO processing ranges from 5 to 100 mS/cm [44]. While, the PEO electrolyte used in this study, had an electrical conductivity of 10.43 mS/cm. The addition of Ag NPs and pure Zn NPs to the electrolyte increased the electrical conductivity to between 12.28 and 13.96 mS/cm, respectively (**Table. 2**). A higher electrical conductivity was due to the additional dissolved ion concentrations from the NPs. It has been found that having a high electrical conductivity in the PEO electrolyte aids the oxide layer formation, as the breakdown voltage required is lower [45], [46].

SLM Ti6Al4V implants have been reported to have an amorphous native TiO₂ layer on the surface (**Figure. 27A**) [47]. In the PEO process, oxidation-reduction reactions induce the thickening of the native oxide layer on the SLM implants surface. As the layer grows (**Figure. 27B**), it acts as an insulator or barrier that restrains the current flow, applied throughout the process. The growth of the native TiO₂ barrier layer occurred in the first 9 ± 1 seconds, as can be observed in the initial high

voltage rate (**Figure. 9**). When the voltage reaches a breakdown value, dielectric breakdowns occur, which is accompanied by plasma discharges (**Figure. 27C**). During dielectric breakdown, the barrier layer is destroyed, followed by the growth of a newly formed TiO₂ layer. The breakdowns allow the electrolyte species and NPs access into the TiO₂ layer. The negative charged NPs will be driven, by the electrophoretic mobility, into the SLM implant surface and trapped in the growing oxide layer. The simultaneous high local temperature from the plasma discharges during breakdown and rapid cooling from the electrolyte promote the crystallization of the amorphous TiO₂ layer into anatase and rutile phases [48], [49]. As the water molecules breakdown due to the high temperature, the resulting oxygen gases are trapped in the TiO₂ layer and form pores on the surface of the SLM implants [50]. Throughout the PEO process, the titanium substrate will continuously be consumed and the TiO₂ layer is synchronously formed and perforated, resulting in a thickened porous TiO₂ surface (**Figure. 27D**).

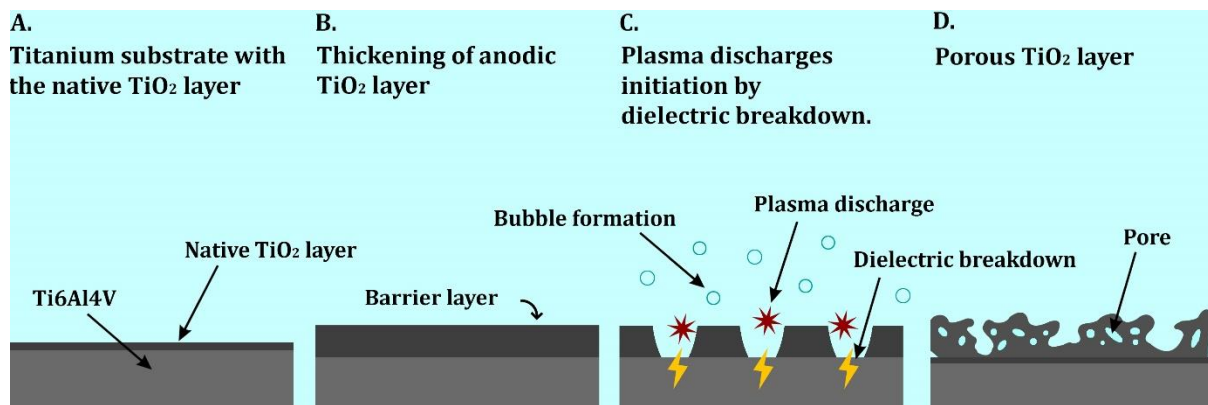


Figure. 27 Illustration of the porous TiO₂ surface formation in PEO process. **A.** Amorphous native TiO₂ layer present on the titanium implant surface. **B.** The thickening of anodic TiO₂ barrier layer as the constant current is applied. **C.** Plasma discharges initiation by dielectric breakdown, creating a channel for fresh electrolyte to enter and interact with the titanium and TiO₂ layer. **D.** Resulting interconnected porous TiO₂ surface.

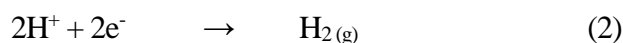
In this study, the entire PEO process was conducted for 300 seconds, and resulted in a uniformly interconnected nano/microporous TiO₂ surface, as identified by SEM images (**Figure. 10**). The V-t transients (**Figure. 9**) demonstrated a similar trend for all implant groups. Although a slightly difference in breakdown voltages was observed (**Table. 3**), it did not affect the surface morphology of the implants but could indicate that the NPs could undergo phase transformation during PEO processing. The differences in breakdown voltages could be caused by the melting temperature of the newly for TiO₂ layer incorporated with NPs [51], [52]. A higher melting temperature of the newly formed TiO₂ layer will result in a higher breakdown voltage required in the PEO process. Pure Zn NPs have a lower melting temperature than Ag NPs. The slightly higher breakdown voltage in the addition of pure Zn NPs compared with Ag NPs suggested that pure Zn NPs might have transformed into

ZnO NPs or other zinc complexes, which have a higher melting temperature than Ag NPs. However, XRD phase analysis on the implant surface was not performed in this study, as the previous study could not detect any NPs complex formations on the implant surface through XRD characterization [36]. Nevertheless, the PEO processing has incorporated the Ag NPs and pure Zn NPs to the SLM implants surface. The NPs were not only found integrated to the surface, but also appeared to be in direct contact among each other, as confirmed by the EDS spot analysis (**Figure. 11** and **12**). The presence of Ag NPs and pure Zn NPs on the biofunctionalized SLM implant surface will provide antibacterial properties, through Ag^+ and Zn^{2+} ion release and $\cdot\text{OH}$ radical generation.

The ion release kinetics from the implants (**Figure. 14**), demonstrated an initial burst of Ag^+ and Zn^{2+} ions in the first 12 hours, followed by a gradual lower ion release for up to 28 days. Interactions of Ag^+ and Zn^{2+} ion release in the implant groups with Ag NPs and pure Zn NPs combinations (**Figure. 15**) expressed a dominant Zn^{2+} ion release in the first 12 hours, whereas a higher Ag^+ ion release took part at the latter time points. Furthermore, the EDS spot analysis, on the implant surface after 24 hours ion releases (**Figure. 16**), not only confirmed that the preferential Zn^{2+} ion release had occurred (leaving a very small number of pure Zn NPs found on the implant surface), but also suggested that in a protection for Ag NPs.

Similar Ag^+ and Zn^{2+} ion release kinetics behavior were also reported by Jin *et al.* [28], [29] on the synergistic potential of dual Ag and Zn ion-implanted titanium. The direct contact between Ag and Zn on the studies provoked micro-galvanic coupling once the substrates were immersed in the physiological saline solution, resulting in the preferential release of Zn^{2+} ions while protecting Ag on the titanium surface. Although the galvanic couplings on the biofunctionalized SLM implants were not measured in this study, the ion release behavior (**Figure. 15**) and EDS spot analysis (**Figure. 16**) results strongly suggest that micro-galvanic coupling occurred between the direct contact of Ag NPs and pure Zn NPs on the biofunctionalized SLM implant surface.

The preferential Zn^{2+} ion release on the implant groups with Ag NPs and pure Zn NPs combinations could be explained due to the standard electrode potential differences between Ag NPs, pure Zn NPs, and TiO_2 surface. Pure Zn NPs, with the lowest electrode potential ($E_{\text{Zn}}^{\circ} = -0.7618 \text{ V}$) act as anode, while Ag NPs and TiO_2 surface serve as cathode ($E_{\text{Ag}}^{\circ} = 0.7996 \text{ V}$) and electron pathway ($E_{\text{TiO}_2}^{\circ} = -0.502 \text{ V}$), respectively [53]. Hence, the pure Zn NPs were oxidized and Zn^{2+} ions were released (**Eq. 1**), while the electrons were transferred through TiO_2 surface and hydrogen gas evolutions occurred in Ag NPs, (**Eq. 2**).



Besides Ag^+ and Zn^{2+} ion release, $\cdot\text{OH}$ radical generations were also detected from all biofunctionalized SLM implant groups. Studies have demonstrated that TiO_2 generated $\cdot\text{OH}$ radical [54]–[56]. Likewise, $\cdot\text{OH}$ radical generation was also found in PT implant (**Figure. 17**). The inclusion of Ag NPs demonstrated an increased $\cdot\text{OH}$ radical generation compared with PT implant (**Figure. 18**). While, the inclusion of pure Zn NPs generated the highest $\cdot\text{OH}$ radicals of all implant groups. This could be due to the interaction between pure Zn NPs and TiO_2 surface that resulted in a higher catalytic activity as both are possible to generate electron–hole pairs [57]. The $\cdot\text{OH}$ radical generations indicated that pure Zn NPs gave more contribution compared with Ag NPs.

The immediate $\cdot\text{OH}$ radical generations, within 10 minutes after the DMPO–PBS solution was added, demonstrated the highest $\cdot\text{OH}$ radical intensity, 0.17 a.u., by PT–Zn. While, PT–Ag Zn 25 75 and PT–Ag Zn 50 50, with a lower pure Zn NPs concentration on the implant surface, were able to generate a comparable $\cdot\text{OH}$ radical intensity, 0.15 and 0.11 a.u., respectively. These results could possibly indicate the direct contact between Ag NPs and pure Zn NPs, not only resulted in preferential of Zn^{2+} ion release, but also in the enhanced immediate $\cdot\text{OH}$ radical generations.

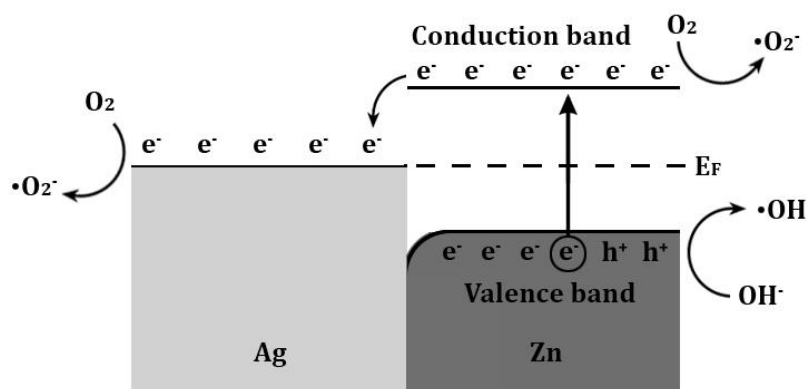


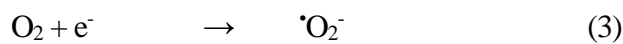
Figure. 28 Enhanced immediate $\cdot\text{OH}$ radical generation in the direct contact between Ag NPs and pure Zn NPs.

The $\cdot\text{OH}$ radical generations and the possible synergism potential (**Figure. 28**) can be explained as following. When pure Zn NPs receive an energy equal or higher than the band gap, electrons from the valence band will be excited to the conduction band and simultaneously leaving holes (h^+) in the valence band. These h^+ can react with hydroxyl ions, forming $\cdot\text{OH}$ radical. The excited electrons in the conduction band have possibilities to recombine with the h^+ , thus will hamper the $\cdot\text{OH}$ radical generation. Several studies have shown that the addition of noble metal, like Ag NPs, in direct contact with pure Zn NPs can overcome this boundary [58]–[61]. During the contact, excited electrons

from pure Zn NPs conduction band will be transferred to Ag NPs driven by the energy level differences. Here, the Ag NPs act as electrons collector, which decreases the possibility for the electron to recombine, resulting in the immediate enhanced $\cdot\text{OH}$ radical generation.

However, the enhanced immediate $\cdot\text{OH}$ radical generation on all implants with Ag NPs and pure Zn NPs combinations did not last longer than 10 minutes. The $\cdot\text{OH}$ radical intensity continuously dropped afterwards. Since the DMPO was dissolved in PBS solution, this kinetic behavior could be explained due to the competition between the $\cdot\text{OH}$ radical generation and the preferential Zn^{2+} ion release. When the $\cdot\text{OH}$ radicals were generated, the simultaneous rapid dissolution of pure Zn NPs was also occurred. Since the pure Zn NPs contributed more in $\cdot\text{OH}$ radical generation, hence, the rapid degradation of pure Zn NPs resulted in a not sufficient concentration of pure Zn NPs on the implant surface to generate $\cdot\text{OH}$ radical at latter time points. Apart from that, a higher pure Zn NPs content on the implant surface resulted in a more immediate $\cdot\text{OH}$ radical generation. The highest to the lowest immediate OH radical generation: PT–Zn > PT–Ag Zn 25 75 > PT–Ag Zn 50 50 > PT–Ag Zn 75 25 > PT–Ag > PT–Ag Zn (**Figure. 18**). Moreover, the Ag NPs concentrations in contact with pure Zn NPs on the implant surface also affected the immediate $\cdot\text{OH}$ radical generation. A high Ag NPs concentration, as in PT–Ag Zn implant, demonstrated almost no enhancement of the immediate $\cdot\text{OH}$ radical generation. Other studies also reported that the addition of a higher than a certain optimal concentration of Ag in contact with Zn could result in a decrease radical generation activity [59], [60].

Besides the $\cdot\text{OH}$ radical generation, $\cdot\text{CH}_3$ radicals were also detected as result of the reactions between acetic ions and the h^+ generated by TiO_2 surface [62]. Also, superoxide radical anions were supposed to be formed due to the interaction between oxygens and the excited electrons in the conduction band (**Eq. 3**). Yet, the superoxide anions spectra were not detected in this study. It was possible that they reacted directly with surrounding water (**Eq. 4-6**), which also resulted in $\cdot\text{OH}$ radical generation.



The addition of Ag NPs and pure Zn NPs on the biofunctionalized SLM implants demonstrated antibacterial properties against MRSA. The synergistic potential of Ag^+ and Zn^{2+} ion release corresponded to the results of the *in vitro* antibacterial leaching activity against MRSA The inhibition zones (**Figure. 19**) of PT–Ag Zn 25 75, PT–Ag Zn 50 50, PT–Ag Zn 75 25, and PT–Ag Zn

implants were comparable with the inhibition zone of PT–Ag, which indicated that the dominant Zn^{2+} ion release concentrations in the first 24 hours were capable to substitute the lesser Ag^+ ion concentrations. Additionally, the Ag^+ and Zn^{2+} ions were observed to possess a synergistic potential in the MIC and MBC results (**Figure. 20**). When Ag^+ and Zn^{2+} ions were combined, a lower concentration from each antibacterial agent were needed to inhibit and kill bacteria.

Antibacterial properties against adherent and non-adherent MRSA were also observed when the implants were incubated with the bacteria. PT–Ag implant and all implant groups with Ag NPs and pure Zn NPs combinations killed the bacteria after 24 hours incubation (**Figure. 21**), while only PT–Ag Zn 75 25, PT–Ag, and PT–Ag Zn killed the non-adherent MRSA (**Figure. 22**). Results demonstrated that PT–Ag Zn 75 25 and PT–Ag Zn implants had similar antibacterial properties as PT–Ag. The high initial release of Zn^{2+} ions in synergism with the low initial Ag^+ ion release on PT–Ag Zn 75 25 and PT–Ag Zn implants (**Table. 4**) were able to kill the non-adherent bacteria. Simultaneously, the protected Ag NPs and $\bullet OH$ radical generation on the implant surface could prevent bacteria to adhere. This results suggested that by substituting 25% of Ag NPs with pure Zn NPs, similar antibacterial properties as PT–Ag could be achieved.

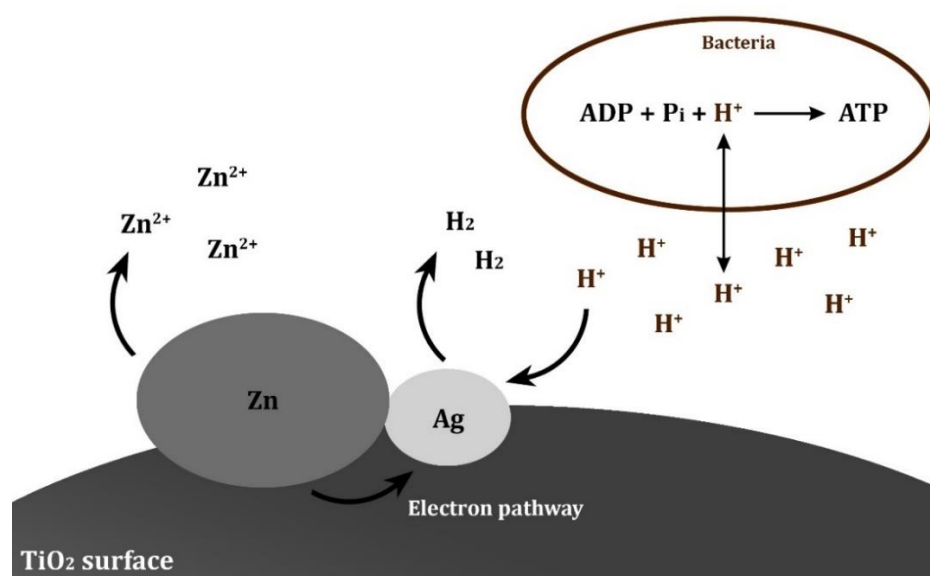


Figure. 29 An illustration of synergistic potential by micro-galvanic coupling, when Ag NPs and pure Zn NPs are in direct contact on TiO_2 surface, leading to a preferential release of Zn^{2+} ions and a H^+ depletion region in the environment which will disrupt the ATP synthesis in bacteria cell.

Besides that, the preferential Zn^{2+} ion release from the implant groups with Ag NPs and pure Zn NPs combinations will also result in a H^+ depletion region in the bacteria surrounding due to the consumption of H^+ during the micro-galvanic coupling (**Eq. 2**). The H^+ depletion region (**Figure. 29**)

is believed to disturb the ATP synthesis and ion transport in bacteria. Since ATP is an essential energy source for bacteria, the inactivation ATP synthesis could lead to bacterial death [63].

To prevent IAI, the biofunctionalized SLM implants were not only required to inhibit bacteria growth and have a bactericidal activity, but also to have antibiofilm properties. PT–Ag implant and all implant groups with Ag NPs and pure Zn NPs combinations demonstrated antibiofilm properties for up to 24 hours, with only few dozen MRSA found inside deep pores. While, MRSA biofilm initiation was found on the NT implant and a significant number of adherent bacteria were observed on PT and PT–Zn implants (**Figure. 23-25**).

Overall, the results have shown that PT–Ag had a stronger antibacterial activity than PT–Zn. Studies have reported that Ag^+ ions have the ability to bind cytoplasmic proteins which disturb the enzyme synthesis and the disruption of DNA replication, which lead to bacteria death [64]–[66], while Zn^{2+} ions only provided bacteriostatic activity [67]. Studies have reported that not only Ag NPs [68], but also Ag^+ ions can also induced $\cdot\text{OH}$ radical generation through the reaction with H_2O_2 produced by the cells [69]–[71], which imply that the $\cdot\text{OH}$ radical generated by PT–Ag could enhance during the incubation with bacteria. Moreover, in TiO_2 surface, Ag NPs also demonstrated a superiority compared to pure Zn NPs due to the differences in the standard electrode potentials. Micro-galvanic coupling between Ag NPs ($E_{\text{Ag}}^0 = 0.7996 \text{ V}$) and TiO_2 surface ($E_{\text{TiO}_2}^0 = -0.502 \text{ V}$) on PT–Ag resulted in protection of Ag NPs and the preferential release of titanium ions [63]. While, the inclusion of pure Zn NPs ($E_{\text{Zn}}^0 = -0.7618 \text{ V}$) into TiO_2 surface, PT–Zn, resulted in faster dissolution of Zn^{2+} ions. The cumulative release of Zn^{2+} ions from PT–Zn (**Figure. 14**), was higher compared to the release of Ag^+ ions from PT–Ag. However, the higher cumulative Zn^{2+} ion release did not present any antibacterial effect but resulted in a faster degradation of pure Zn NPs, leaving the implant surface unprotected. Studies also have demonstrated that Zn^{2+} ions play a role in cellular interaction among *Staphylococci* which responsible for the bacterial adhesion and biofilm formation [72], [73]. Zn^{2+} ions are important elements for cells, including bacteria, and involve in metabolic activities, such as ATP synthesis [74], which also explained that why PT–Zn is less toxic than PT–Ag.

PT–Zn implants did not demonstrate any antibacterial effect against MRSA. Although the MIC and MBC results indicated that Zn^{2+} ions alone possess antibacterial properties, however, the required Zn^{2+} ion concentration was very high. The MIC and MBC of Zn^{2+} ions were 20 and 40 times higher, respectively, compared to Ag^+ ions. The 24 hours Zn^{2+} ion release concentration from the PT–Zn was 861.3 ppb, which was comparable to the Ag^+ ion release from PT–Ag, 860.5 ppb. This explained that the Zn^{2+} ion release concentration from PT–Zn was not enough to show any inhibition zone and antibacterial effect when incubated with MRSA. Although it is possible to show its

antibacterial properties by synthesizing a higher pure Zn NPs concentration on the implant, but the resulting implant would most likely become cytotoxic towards osteoblasts. Yamamoto *et al.* [75] reported the cytotoxic concentration of ZnCl_2 towards murine osteoblastic cells (MC3T3-E1) starting from 0.09 mM. While, the MBC of $\text{Zn}(\text{NO}_3)_2$ required to kill MRSA was much higher, 10 mM. Nonetheless, many studies have reported that the addition of Zn elements on titanium substrate would induce osteogenesis [76]–[78]. Hence, the strategy to combine Ag NPs and pure Zn NPs on the implant surface for its antibacterial as well as osteogenic properties is promising for further research.

4.2. Recommendations for future work

Antibacterial surface bearing Ag NPs and pure Zn NPs have been synthesized on porous SLM implant through a single step PEO surface modification technique. Synergistic potentials between the Ag NPs and pure Zn NPs also showed promising *in vitro* antibacterial properties against MRSA. Future studies should consider to:

- Identify the phase compositions of the Ag NPs and pure Zn NPs attached on implant surface using high-resolution transmission electron microscopy (HRTEM).
- Measure the corrosion potential and current density of the implants with Ag NPs and pure Zn NPs combinations to determine the micro-galvanic coupling on the implants surface.
- Investigate the type direct contact interaction between Ag NPs and pure Zn NPs on the implant surface using HRTEM. For example, are the pure Zn NPs covered the Ag NPs, or vice versa, or are they merely attached on the implant surface next to one another. Since the synergism potential by micro-galvanic coupling occurred when Ag NPs were in direct contact with pure Zn NPs, the contact area became important and could result in different *in vitro* antibacterial and osteogenic properties as reported by Jin *et al.* [29].
- Observe the time killing activity against MRSA. Results have shown that Zn^{2+} ion release took part in the early hours and Ag^+ ion release increased in the latter time. Hence, this antibacterial assay could be taken into consideration to observe how does the bacteria viability over time related with the synergism potential of the ion release.
- Involve the fluorescence assay for the biofilm formation experiment. Therefore, the alive or dead adherent bacteria on the implant surface can be clearly differentiate.
- Assess the *in vitro* antibacterial properties against other pathogenic *Staphylococci* strains, such as *S. epidermidis*, and other coagulase negative *Staphylococci*. Those bacteria were the major causative pathogenic in IAI, which also developed resistance towards antibiotics [12].
- Test the *in vitro* cytotoxicity with human MSCs. So that, the appropriate Ag NPs and pure Zn NPs concentration on the implant surface can be tuned, not only for antibacterial properties, but also to support bone formation.
- Proceed to *ex vivo* and *in vivo* studies.

5 Conclusions

Antibacterial surfaces of porous SLM Ti6Al4V implants have been biofunctionalized using PEO. The resulting porous TiO₂ surface contained Ag NPs and pure Zn NPs, which were able to release Ag⁺ and Zn²⁺ ion release for at least 28 days and generate [•]OH radical for 150 minutes. All implant groups, except PT–Zn, have shown *in vitro* antibacterial leaching activity, as well as *in vitro* prevention against MRSA biofilm formation for at least 24 hours. Only PT–Ag Zn 75 25 and PT–Ag Zn demonstrated similar bactericidal properties, as PT–Ag, against adherent and non-adherent MRSA. The results suggested that by substituting 25% of Ag NPs with pure Zn NPs, similar antibacterial properties as PT–Ag could be achieved. The antibacterial mechanism of preferential Zn²⁺ ion release in synergism with a lower concentration of Ag⁺ ion release, at the first 24 hours, is believed to eradicate the non-adherent MRSA. While, the protected Ag NPs on the surface in the first 24 hours and the [•]OH radical generations prevent MRSA adhesion and biofilm formation on the implant surface. Altogether, this study demonstrated the synergistic antibacterial properties of Ag NPs and pure Zn NPs on porous SLM titanium implants to prevent IAI.

6 Acknowledgements

"I would first like to thank my supervisor Dr. Ir. Iulian Apachitei, whose door was always open when I needed guidance, but also allowed me the freedom to work independently on this project. Throughout my thesis, I also had the full support of my daily supervisor, Ir. Ingmar van Hengel, who has helped me with both my project and my thesis report.

I would also like to acknowledge Sander Leeftang for his technical support, Yageng Li for training me on the SEM, Ruud Hendrikx for helping me with the XRD measurements, and Michel van den Brink for conducting the ICP-OES measurements. A special thanks to Dr. Peter-Leon Hagedoorn, who assisted me during the EPR measurements. Lastly, I would like to thank Melissa Tierolf for helping me with antibacterial testing at University Medical Center Utrecht."

7 Abbreviations

CAMH	–	Cation-adjusted Mueller Hinton
CFU	–	Colony forming unit
DLVO	–	Derjaguin Landau Verwey and Overbeek
DMPO	–	Dimethyl-pyrroline N-oxide
EDS	–	Energy dispersive X-ray spectroscopy
EPR	–	Electron paramagnetic resonance
HRTEM	–	High-resolution transmission electron microscopy
IAI	–	Implant-associated infection
ICP-OES	–	Inductively coupled plasma-optical emission spectrometry
LB	–	Luria-Bertani
MBC	–	Minimum bactericidal concentration
MIC	–	Minimum inhibitory concentration
MRSA	–	Methicillin-resistant <i>staphylococcus aureus</i>
MSCs	–	Mesenchymal stem cells
NPs	–	nanoparticles
NT	–	Non-treated
OD _{600nm}	–	Optical density at 600 nm wavelength
PEO	–	Plasma electrolytic oxidation
PT	–	PEO-treated
RPM	–	Rotation per minute
SEM	–	Scanning electron microscopy
SLM	–	Selective laser melting
THA	–	Total hip arthroplasty
TiO ₂	–	Titanium oxide
TKA	–	Total knee arthroplasty
TSB	–	Tryptic soy broth
V-t	–	Voltage-time
XRD	–	X-ray diffraction

8 References

- [1] J. Parvizi, V. Aggarwal, and M. Rasouli, “Periprosthetic joint infection: Current concept,” *Indian J. Orthop.*, vol. 47, no. 1, p. 10, 2013.
- [2] D. Culliford, J. Maskell, A. Judge, C. Cooper, D. Prieto-Alhambra, and N. K. Arden, “Future projections of total hip and knee arthroplasty in the UK: Results from the UK Clinical Practice Research Datalink,” *Osteoarthr. Cartil.*, vol. 23, no. 4, pp. 594–600, 2015.
- [3] D. A. Register, “LROI - Annual Report,” 2017.
- [4] S. Nemes, M. Gordon, C. Rogmark, and O. Rolfson, “Projections of total hip replacement in Sweden from 2013 to 2030,” *Acta Orthop.*, vol. 85, no. 3, pp. 238–243, 2014.
- [5] J. Gallo, M. Kolár, R. Novotný, P. Riháková, and V. Tichá, “Pathogenesis of prosthesis-related infection,” *Biomed. Pap. Med. Fac. Univ. Palacky. Olomouc. Czech. Repub.*, vol. 147, no. 1, pp. 27–35, 2003.
- [6] S. J. McConoughey *et al.*, “Biofilms in periprosthetic orthopedic infections,” *Future Microbiol.*, vol. 9, no. 8, pp. 987–1007, 2014.
- [7] C. R. Arciola, D. Campoccia, P. Speziale, L. Montanaro, and J. W. Costerton, “Biofilm formation in Staphylococcus implant infections. A review of molecular mechanisms and implications for biofilm-resistant materials,” *Biomaterials*, vol. 33, no. 26, pp. 5967–5982, 2012.
- [8] W. Zimmerli, “Clinical presentation and treatment of orthopaedic implant-associated infection,” *J. Intern. Med.*, vol. 276, no. 2, pp. 111–119, 2014.
- [9] E. M. Hetrick and M. H. Schoenfisch, “Reducing implant-related infections: active release strategies,” *Chem. Soc. Rev.*, vol. 35, no. 9, p. 780, 2006.
- [10] S. M. Odum *et al.*, “Irrigation and debridement for periprosthetic infections: Does the organism matter?,” *J. Arthroplasty*, vol. 26, no. SUPPL. 6, pp. 114–118, 2011.
- [11] N. Høiby *et al.*, “The clinical impact of bacterial biofilms,” *Int. J. Oral Sci.*, vol. 3, no. 2, pp. 55–65, 2011.
- [12] D. Campoccia, L. Montanaro, and C. R. Arciola, “The significance of infection related

- to orthopedic devices and issues of antibiotic resistance,” *Biomaterials*, vol. 27, no. 11, pp. 2331–2339, 2006.
- [13] V. K. Aggarwal, H. Bakhshi, N. U. nter Ecker, J. Parvizi, T. Gehrke, and D. Kendoff, “Organism profile in periprosthetic joint infection: pathogens differ at two arthroplasty infection referral centers in Europe and in the United States,” *J. Knee Surg.*, vol. 27, no. 5, pp. 399–406, 2014.
- [14] T. Ferry *et al.*, “Risk factors for treatment failure in orthopedic device-related methicillin-resistant *Staphylococcus aureus* infection,” *Eur. J. Clin. Microbiol. Infect. Dis.*, vol. 29, no. 2, pp. 171–180, 2010.
- [15] M. F. Kurd, E. Ghanem, J. Steinbrecher, and J. Parvizi, “Two-stage exchange knee arthroplasty: Does resistance of the infecting organism influence the outcome?,” *Clin. Orthop. Relat. Res.*, vol. 468, no. 8, pp. 2060–2066, 2010.
- [16] F. Leung, C. J. Richards, D. S. Garbuz, B. A. Masri, and C. P. Duncan, “Two-stage total hip arthroplasty: How often does it control methicillin-resistant infection?,” *Clin. Orthop. Relat. Res.*, vol. 469, no. 4, pp. 1009–1015, 2011.
- [17] J. T. Seil and T. J. Webster, “Antimicrobial applications of nanotechnology: Methods and literature,” *Int. J. Nanomedicine*, vol. 7, pp. 2767–2781, 2012.
- [18] N. V. Ayala-Núñez, H. H. Lara Villegas, L. Del Carmen Ixtepan Turrent, and C. Rodríguez Padilla, “Silver nanoparticles toxicity and bactericidal effect against methicillin-resistant *staphylococcus aureus*: Nanoscale does matter,” *Nanobiotechnology*, vol. 5, no. 1–4, pp. 2–9, 2009.
- [19] M. K. Rai, S. D. Deshmukh, A. P. Ingle, and A. K. Gade, “Silver nanoparticles: The powerful nanoweapon against multidrug-resistant bacteria,” *J. Appl. Microbiol.*, vol. 112, no. 5, pp. 841–852, 2012.
- [20] G. Franci *et al.*, “Silver nanoparticles as potential antibacterial agents,” *Molecules*, vol. 20, no. 5, pp. 8856–8874, 2015.
- [21] B. S. Necula, L. E. Fratila-Apachitei, S. A. J. Zaat, I. Apachitei, and J. Duszcyk, “In vitro antibacterial activity of porous TiO₂ -Ag composite layers against methicillin-resistant *Staphylococcus aureus*,” *Acta Biomater.*, vol. 5, no. 9, pp. 3573–3580, 2009.
- [22] N. Jones, B. Ray, K. T. Ranjit, and A. C. Manna, “Antibacterial activity of ZnO nanoparticle suspensions on a broad spectrum of microorganisms,” *FEMS Microbiol.*

- Lett.*, vol. 279, no. 1, pp. 71–76, 2008.
- [23] A. Sirelkhatim *et al.*, “Review on zinc oxide nanoparticles: Antibacterial activity and toxicity mechanism,” *Nano-Micro Lett.*, vol. 7, no. 3, pp. 219–242, 2015.
- [24] A. Jesline, N. P. John, P. M. Narayanan, C. Vani, and S. Murugan, “Antimicrobial activity of zinc and titanium dioxide nanoparticles against biofilm-producing methicillin-resistant *Staphylococcus aureus*,” *Appl. Nanosci.*, vol. 5, no. 2, pp. 157–162, 2015.
- [25] U. Kadiyala, E. S. Turali-Emre, J. H. Bahng, N. A. Kotov, and J. Scott Vaneppps, “Unexpected insights into antibacterial activity of zinc oxide nanoparticles against methicillin resistant: *Staphylococcus aureus* (MRSA),” *Nanoscale*, vol. 10, no. 10, pp. 4927–4939, 2018.
- [26] H. Hu, W. Zhang, Y. Qiao, X. Jiang, X. Liu, and C. Ding, “Antibacterial activity and increased bone marrow stem cell functions of Zn-incorporated TiO₂ coatings on titanium,” *Acta Biomater.*, vol. 8, no. 2, pp. 904–915, 2012.
- [27] G. Jin, H. Cao, Y. Qiao, F. Meng, H. Zhu, and X. Liu, “Osteogenic activity and antibacterial effect of zinc ion implanted titanium,” *Colloids Surfaces B Biointerfaces*, vol. 117, pp. 158–165, 2014.
- [28] G. Jin *et al.*, “Synergistic effects of dual Zn/Ag ion implantation in osteogenic activity and antibacterial ability of titanium,” *Biomaterials*, vol. 35, no. 27, pp. 7699–7713, 2014.
- [29] G. Jin *et al.*, “Zn/Ag micro-galvanic couples formed on titanium and osseointegration effects in the presence of *S.aureus*,” *Biomaterials*, vol. 65, pp. 22–31, 2015.
- [30] L. Zhang, Q. Gao, and Y. Han, “Zn and Ag Co-doped Anti-microbial TiO₂ Coatings on Ti by Micro-arc Oxidation,” *J. Mater. Sci. Technol.*, vol. 32, no. 9, pp. 919–924, 2016.
- [31] S. Hackenberg *et al.*, “Silver nanoparticles: Evaluation of DNA damage, toxicity and functional impairment in human mesenchymal stem cells,” *Toxicol. Lett.*, vol. 201, no. 1, pp. 27–33, 2011.
- [32] P. Ickrath *et al.*, “Time-dependent toxic and genotoxic effects of zinc oxide nanoparticles after long-term and repetitive exposure to human mesenchymal stem cells,” *Int. J. Environ. Res. Public Health*, vol. 14, no. 12, 2017.

- [33] A. A. Zadpoor, “Bone tissue regeneration: the role of scaffold geometry,” *Biomater. Sci.*, vol. 3, no. 2, pp. 231–245, 2015.
- [34] N. Taniguchi *et al.*, “Effect of pore size on bone ingrowth into porous titanium implants fabricated by additive manufacturing: An in vivo experiment,” *Mater. Sci. Eng. C*, vol. 59, pp. 690–701, 2016.
- [35] B. S. Necula, I. Apachitei, L. E. Fratila-Apachitei, E. J. Van Langelaan, and J. Duszczyk, “Titanium bone implants with superimposed micro/nano-scale porosity and antibacterial capability,” *Appl. Surf. Sci.*, vol. 273, pp. 310–314, 2013.
- [36] I. A. J. van Hengel *et al.*, “Selective laser melting porous metallic implants with immobilized silver nanoparticles kill and prevent biofilm formation by methicillin-resistant *Staphylococcus aureus*,” *Biomaterials*, vol. 140, pp. 1–15, 2017.
- [37] B. S. Necula, I. Apachitei, F. D. Tichelaar, L. E. Fratila-Apachitei, and J. Duszczyk, “An electron microscopical study on the growth of TiO₂-Ag antibacterial coatings on Ti6Al7Nb biomedical alloy,” *Acta Biomater.*, vol. 7, no. 6, pp. 2751–2757, 2011.
- [38] Y. Agrawal and V. Patel, “Nanosuspension: An approach to enhance solubility of drugs,” *J. Adv. Pharm. Technol. Res.*, vol. 2, no. 2, p. 81, 2011.
- [39] G. R. Buettner, “Spin Trapping - Electron-Spin-Resonance Parameters of Spin Adducts,” *Free Radic. Bio. Med.*, vol. 3, no. 4, pp. 259–303, 1987.
- [40] B. D. Cullity, *Elements of Diffraction*. 1978.
- [41] L. Saunders, “Surface and Colloid Chemistry,” *J. Pharm. Pharmacol.*, vol. 3, no. 1, pp. 865–882, 1951.
- [42] S. Bhattacharjee, “DLS and zeta potential - What they are and what they are not?,” *J. Control. Release*, vol. 235, pp. 337–351, 2016.
- [43] K. M. Kim *et al.*, “Surface treatment of silica nanoparticles for stable and charge-controlled colloidal silica,” *Int. J. Nanomedicine*, vol. 9, pp. 29–40, 2014.
- [44] T. W. Clyne and S. C. Troughton, “A review of recent work on discharge characteristics during plasma electrolytic oxidation of various metals,” *Int. Mater. Rev.*, vol. 0, no. 0, pp. 1–36, 2018.
- [45] S. Ikonopisov, “Theory of electrical breakdown during formation of barrier anodic films,” *Electrochim. Acta*, vol. 22, no. 10, pp. 1077–1082, 1977.

- [46] S. Ono, S. Moronuki, Y. Mori, A. Koshi, J. Liao, and H. Asoh, "Effect of Electrolyte Concentration on the Structure and Corrosion Resistance of Anodic Films Formed on Magnesium through Plasma Electrolytic Oxidation," *Electrochim. Acta*, vol. 240, pp. 415–423, 2017.
- [47] J. Vaithilingam *et al.*, "Surface chemistry of Ti6Al4V components fabricated using selective laser melting for biomedical applications," *Mater. Sci. Eng. C*, vol. 67, pp. 294–303, 2016.
- [48] A. L. Yerokhin, X. Nie, A. Leyland, and A. Matthews, "Characterisation of oxide films produced by plasma electrolytic oxidation of a Ti–6Al–4V alloy," *Surf. Coatings Technol.*, vol. 130, pp. 195–206, 2000.
- [49] H. Habazaki, M. Uozumi, H. Konno, K. Shimizu, P. Skeldon, and G. E. Thompson, "Crystallization of anodic titania on titanium and its alloys," *Corros. Sci.*, vol. 45, no. 9, pp. 2063–2073, 2003.
- [50] E. Matykina, A. Berkani, P. Skeldon, and G. E. Thompson, "Real-time imaging of coating growth during plasma electrolytic oxidation of titanium," *Electrochim. Acta*, vol. 53, no. 4, pp. 1987–1994, 2007.
- [51] M. Tang, Z. Feng, G. Li, Z. Zhang, and R. Zhang, "High-corrosion resistance of the microarc oxidation coatings on magnesium alloy obtained in potassium fluotitanate electrolytes," *Surf. Coatings Technol.*, vol. 264, pp. 105–113, 2015.
- [52] S. Fatimah, M. P. Kamil, J. H. Kwon, M. Kaseem, and Y. G. Ko, "Dual incorporation of SiO₂ and ZrO₂ nanoparticles into the oxide layer on 6061 Al alloy via plasma electrolytic oxidation: Coating structure and corrosion properties," *J. Alloys Compd.*, vol. 707, pp. 358–364, 2017.
- [53] P. Vanýsek, "Electrochemical Series," *CRC Handb. Chem. Physics, 87th Ed.*, pp. 1–10, 2005.
- [54] I. Fenoglio, G. Greco, S. Livraghi, and B. Fubini, "Non-UV-induced radical reactions at the surface of TiO₂ nanoparticles that may trigger toxic responses," *Chem. - A Eur. J.*, vol. 15, no. 18, pp. 4614–4621, 2009.
- [55] J. J. Yin *et al.*, "Phototoxicity of nano titanium dioxides in HaCaT keratinocytes- Generation of reactive oxygen species and cell damage," *Toxicol. Appl. Pharmacol.*, vol. 263, no. 1, pp. 81–88, 2012.

- [56] A. Lipovsky, L. Levitski, Z. Tzitrinovich, A. Gedanken, and R. Lubart, "The different behavior of rutile and anatase nanoparticles in forming oxy radicals upon illumination with visible light: An EPR study," *Photochem. Photobiol.*, vol. 88, no. 1, pp. 14–20, 2012.
- [57] R. Dhanalakshmi, A. Pandikumar, K. Sujatha, and P. Gunasekaran, "Photocatalytic and antimicrobial activities of functionalized silicate sol–gel embedded ZnO–TiO₂ nanocomposite materials," *Mater. Express*, vol. 3, no. 4, pp. 291–300, 2013.
- [58] Y. Zheng, L. Zheng, Y. Zhan, X. Lin, Q. Zheng, and K. Wei, "Ag/ZnO heterostructure nanocrystals: Synthesis, characterization, and photocatalysis," *Inorg. Chem.*, vol. 46, no. 17, pp. 6980–6986, 2007.
- [59] W. Lu, S. Gao, and J. Wang, "One-Pot Synthesis of Ag / ZnO Self-Assembled 3D Hollow Microspheres with Enhanced Photocatalytic Performance," *Society*, pp. 16792–16800, 2008.
- [60] O. Bechambi, M. Chalbi, W. Najjar, and S. Sayadi, "Photocatalytic activity of ZnO doped with Ag on the degradation of endocrine disrupting under UV irradiation and the investigation of its antibacterial activity," *Appl. Surf. Sci.*, vol. 347, pp. 414–420, 2015.
- [61] Z. Li, F. Zhang, A. Meng, C. Xie, and J. Xing, "ZnO/Ag micro/nanospheres with enhanced photocatalytic and antibacterial properties synthesized by a novel continuous synthesis method," *RSC Adv.*, vol. 5, no. 1, pp. 612–620, 2015.
- [62] I. R. MacDonald, S. Rhydderch, E. Holt, N. Grant, J. M. D. Storey, and R. F. Howe, "EPR studies of electron and hole trapping in titania photocatalysts," *Catal. Today*, vol. 182, no. 1, pp. 39–45, 2012.
- [63] H. Cao, X. Liu, F. Meng, and P. K. Chu, "Biological actions of silver nanoparticles embedded in titanium controlled by micro-galvanic effects," *Biomaterials*, vol. 32, no. 3, pp. 693–705, 2011.
- [64] T. C. Dakal, A. Kumar, R. S. Majumdar, and V. Yadav, "Mechanistic basis of antimicrobial actions of silver nanoparticles," *Front. Microbiol.*, vol. 7, no. NOV, pp. 1–17, 2016.
- [65] L. Wang, C. Hu, and L. Shao, "The antimicrobial activity of nanoparticles: present situation and prospects for the future," *Int J Nanomedicine*, vol. 12, pp. 1227–1249,

- 2017.
- [66] M. Rai *et al.*, “Broadening the spectrum of small-molecule antibacterials by metallic nanoparticles to overcome microbial resistance,” *Int. J. Pharm.*, vol. 532, no. 1, pp. 139–148, 2017.
- [67] D. Chudobova *et al.*, “The effect of metal ions on *Staphylococcus aureus* revealed by biochemical and mass spectrometric analyses,” *Microbiol. Res.*, vol. 170, pp. 147–156, 2015.
- [68] W. Zhang, Y. Li, J. Niu, and Y. Chen, “Photogeneration of reactive oxygen species on uncoated silver, gold, nickel, and silicon nanoparticles and their antibacterial effects,” *Langmuir*, vol. 29, no. 15, pp. 4647–4651, 2013.
- [69] W. He, Y. T. Zhou, W. G. Wamer, M. D. Boudreau, and J. J. Yin, “Mechanisms of the pH dependent generation of hydroxyl radicals and oxygen induced by Ag nanoparticles,” *Biomaterials*, vol. 33, no. 30, pp. 7547–7555, 2012.
- [70] D. He, S. Garg, and T. D. Waite, “H₂O₂-mediated oxidation of zero-valent silver and resultant interactions among silver nanoparticles, silver ions, and reactive oxygen species,” *Langmuir*, vol. 28, no. 27, pp. 10266–10275, 2012.
- [71] D. He, C. J. Miller, and T. D. Waite, “Fenton-like zero-valent silver nanoparticle-mediated hydroxyl radical production,” *J. Catal.*, vol. 317, pp. 198–205, 2014.
- [72] D. G. Conrady, C. C. Brescia, K. Horii, A. A. Weiss, D. J. Hassett, and A. B. Herr, “A zinc-dependent adhesion module is responsible for intercellular adhesion in staphylococcal biofilms,” *Proc. Natl. Acad. Sci.*, vol. 105, no. 49, pp. 19456–19461, 2008.
- [73] J. A. Geoghegan *et al.*, “Role of surface protein SasG in biofilm formation by *Staphylococcus aureus*,” *J. Bacteriol.*, vol. 192, no. 21, pp. 5663–5673, 2010.
- [74] A. Atkinson and D. R. Winge, “Metal acquisition and availability in the mitochondria,” *Chem. Rev.*, vol. 109, no. 10, pp. 4708–4721, 2009.
- [75] A. Yamamoto, R. Honma, and M. Sumita, “Cytotoxicity evaluation of 43 metal salts using murine fibroblasts and osteoblastic cells,” *J. Biomed. Mater. Res.*, vol. 39, no. 2, pp. 331–340, 1998.
- [76] K. Yusa, O. Yamamoto, M. Fukuda, S. Koyota, Y. Koizumi, and T. Sugiyama, “In vitro

- prominent bone regeneration by release zinc ion from Zn-modified implant,” *Biochem. Biophys. Res. Commun.*, vol. 412, no. 2, pp. 273–278, 2011.
- [77] Z. Zhang, B. Gu, W. Zhang, G. Kan, and J. Sun, “The enhanced characteristics of osteoblast adhesion to porous Zinc-TiO₂ coating prepared by plasma electrolytic oxidation,” *Appl. Surf. Sci.*, vol. 258, no. 17, pp. 6504–6511, 2012.
- [78] Y. Qiao *et al.*, “Stimulation of bone growth following zinc incorporation into biomaterials,” *Biomaterials*, vol. 35, no. 25, pp. 6882–6897, 2014.

9 Appendices



Figure. 30 The as-manufactured porous SLM Ti6Al4V implant.



Figure. 31 Porous SLM Ti6Al4V implants **A.** Before PEO processing and **B.** After PEO processing without NPs, **C-G.** with Ag NPs and pure Zn NPs.



Figure. 32 Calcium and phosphorus-based electrolyte for PEO processing with Ag NPs and pure Zn NPs.

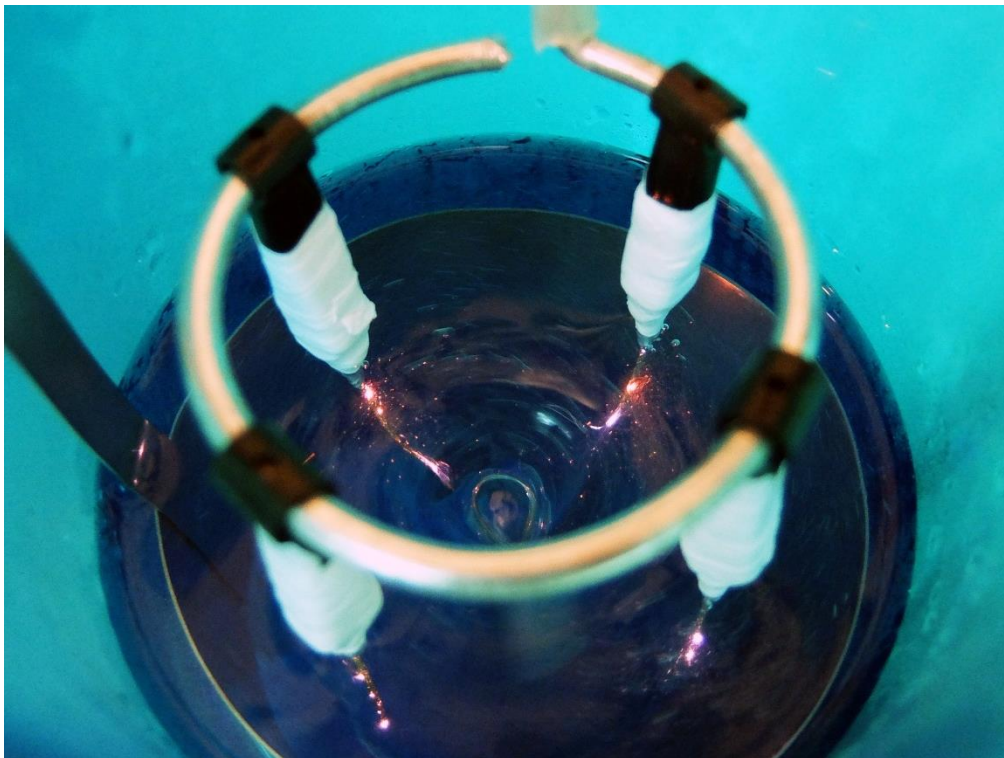
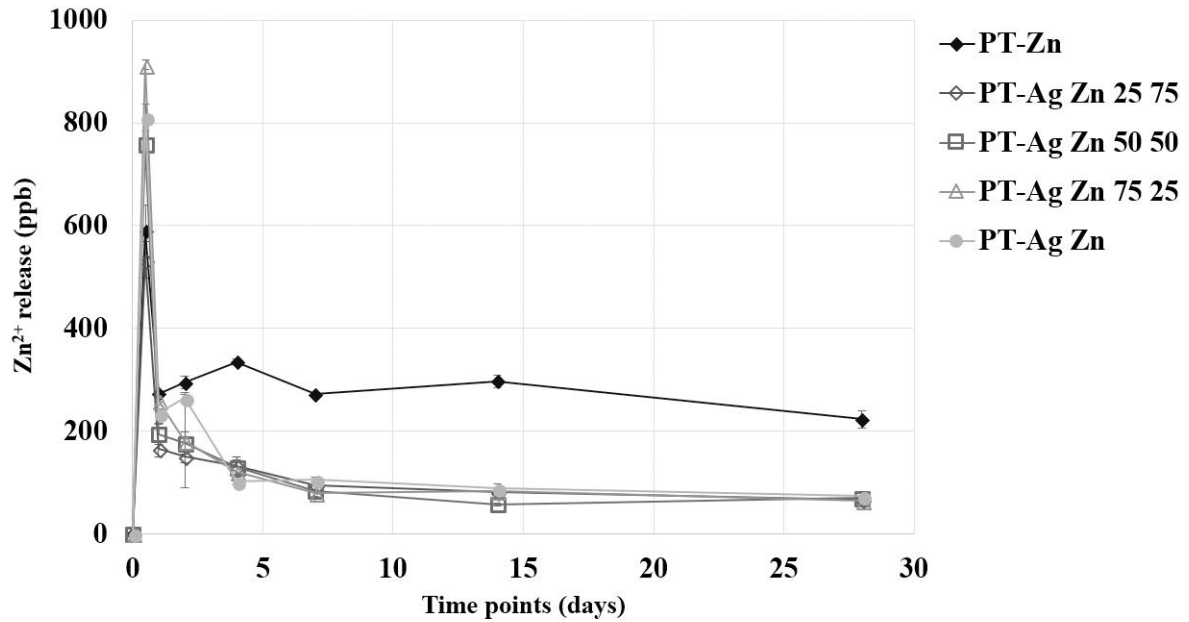


Figure. 33 Plasma discharges occurred throughout the implant surface during PEO processing.

A. Non-cumulative Zn²⁺ release



B. Non-cumulative Ag⁺ release

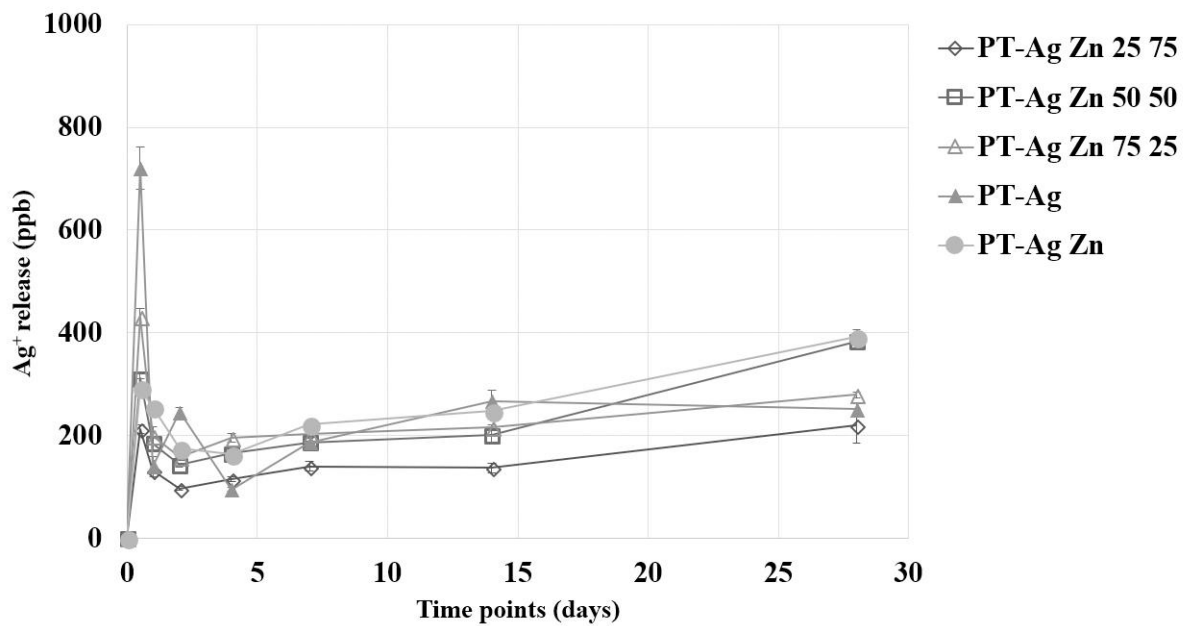


Figure. 34 Non-cumulative release kinetics of **A.** Zn²⁺ and **B.** Ag⁺ ions from the biofunctionalized SLM implants.

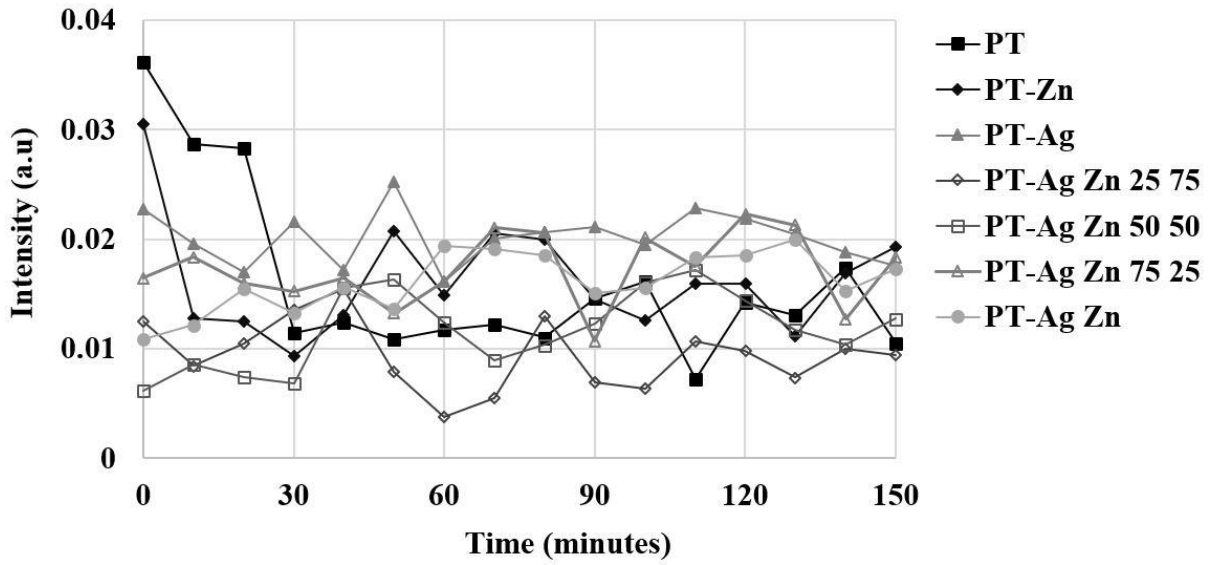


Figure. 35 $^3\text{CH}_3$ radical intensity generated by PEO-treated implants submerged in 20 mM DMPO–PBS solution over 150 minutes.

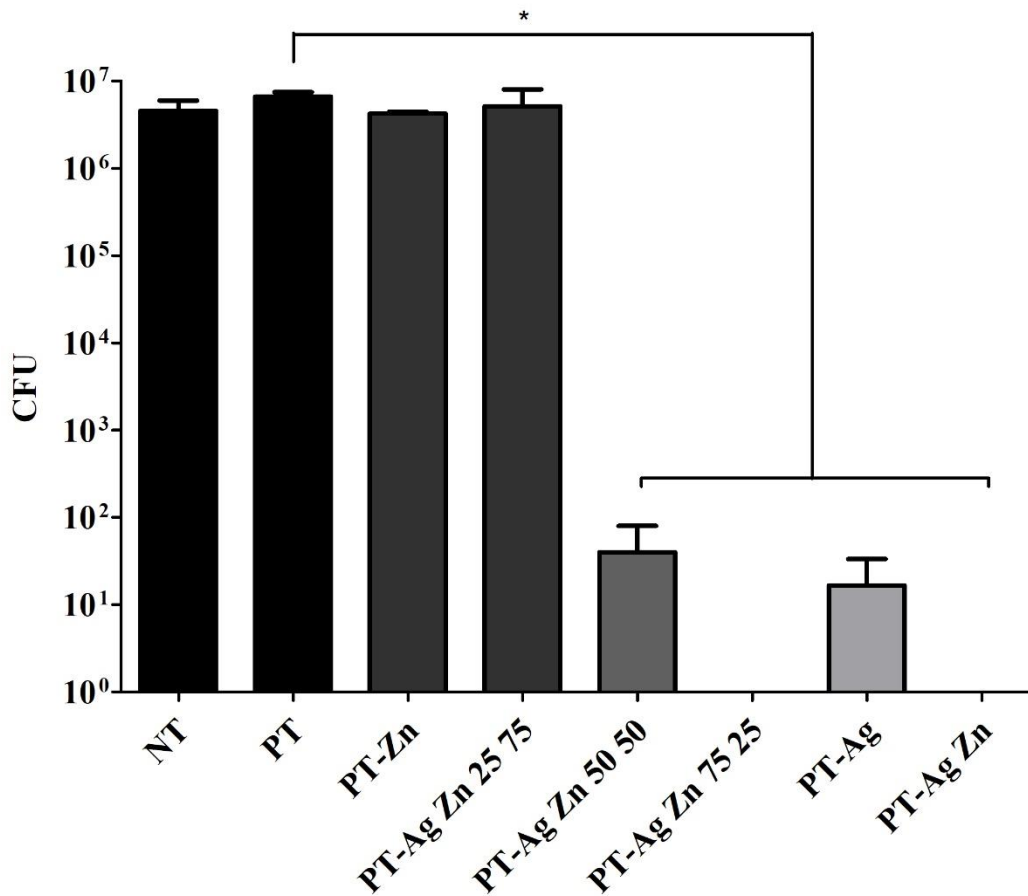


Figure. 36 Bactericidal activity of biofunctionalized SLM implants against adherent MRSA USA300, after overnight incubation with 10^3 CFU MRSA. $n=3$ per group. * $p<0.05$.

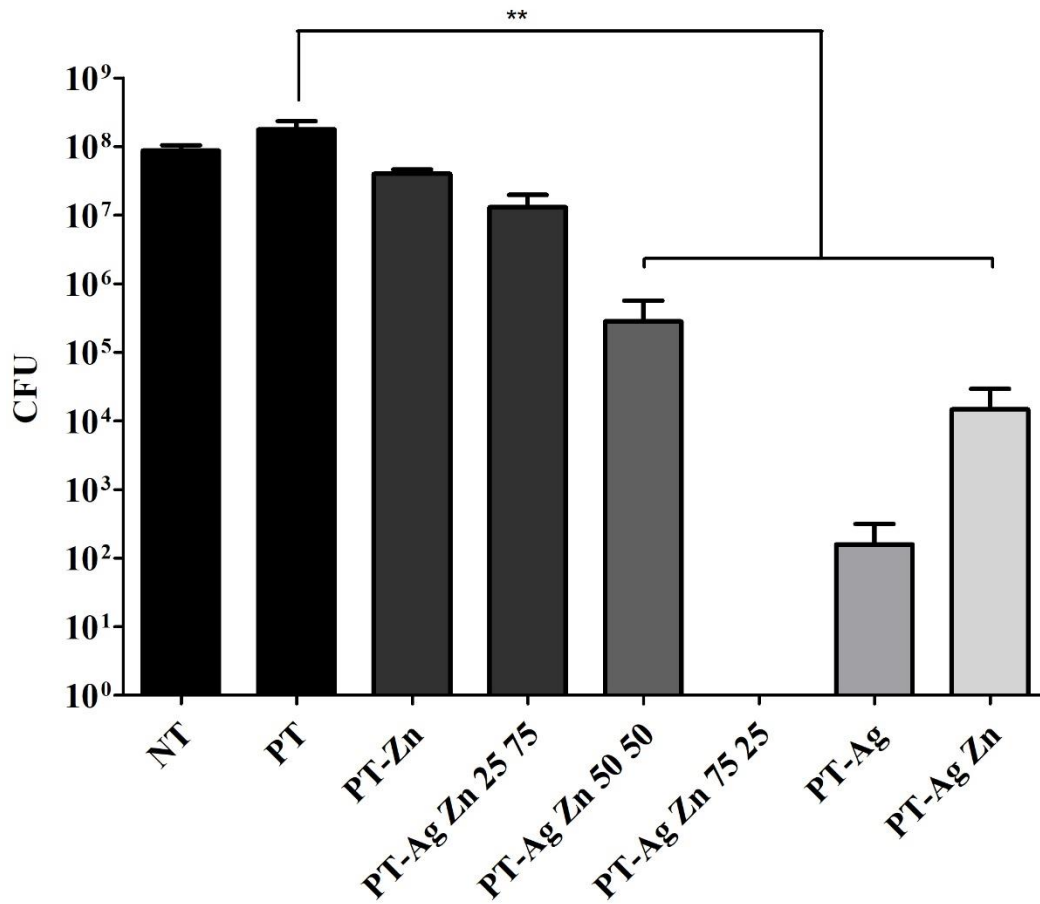


Figure. 37 Bactericidal activity of biofunctionalized SLM implants against non-adherent MRSA USA300, after overnight incubation with 10³ CFU MRSA. n=3 per group. ** p<0.01.